Received: 3 October 2020 | Revised: 8 April 2021 | Accepted: 23 June 2021

DOI: 10.1002/we.2669

RESEARCH ARTICLE

WILEY

A new wake-merging method for wind-farm power prediction in the presence of heterogeneous background velocity fields

Luca Lanzilao | Johan Meyers

Department of Mechanical Engineering, KU Leuven, Leuven, Belgium

Correspondence
Luca Lanzilao, Department of Mechanical Engineering, KU Leuven, Leuven, Belgium.
luca.lanzilao@kuleuven.be

Funding information
Belgian Federal Public Service for Economy, SMEs, and Energy; Fonds Wetenschappelijk Onderzoek, Grant/Award Number: G0B1518N

Abstract

The difference in surface roughness between land and sea, and the terrain complexities, lead to spatially heterogeneous atmospheric conditions, and therefore affect the propagation and dynamics of wind-turbine and wind-farm wakes. Currently, these flow heterogeneities and their effects on plant aerodynamics are not modeled in the majority of engineering wake models. In this study, we address this issue by developing a new wake-merging method capable of superimposing the waked flow on a heterogeneous background velocity field. We couple the proposed wake-merging method with four different wake models, i.e. the Gaussian, super-Gaussian, double-Gaussian and Ishihara model, and we test its performance against LES results, dual-Doppler radar measurements and SCADA data from the Horns Rev, London Array, and Westermost Rough farms. The standard Jensen model with quadratic superposition is also included. In homogeneous conditions, the new method predicts slightly higher velocity deficits than the linear superposition method. Overall, the distributions of the difference in power ratio between the two wake-merging methods predictions and observations show a similar mean absolute error (MAE) and interquartile range (IQR) in such conditions. On the other hand, the new wake-merging method predictions display a lower MAE with a similar IQR in case of a spatially varying background velocity, being overall more accurate than the ones obtained with linear superposition. The most accurate estimates are obtained when the wake-merging methods are coupled with the double-Gaussian and Gaussian single-wake models. In contrast, the Jensen and super-Gaussian wake models overestimate the velocity deficits for the majority of cases analyzed.

KEYWORDS
analytical wake model, coastal gradient, wake-merging method, wakes, wind-farm power prediction

1 | INTRODUCTION

The majority of offshore wind farms are placed near coastal regions to minimize cabling costs and leverage fixed-bottom technology at shallower depths of water. Moreover, due to the current expansion of wind power capacity, the construction of onshore wind farms on non-flat complex terrains is common practice. The different surface roughness and temperature found over land and sea and the flow obstructions caused by

orographic features account for the development of strong horizontal velocity gradients.[1–4] Moreover, nowadays few wind farms much further from the coast are also in operation (see, e.g., the Hornsea wind farm). For these sites the wind speed gradients across the area may not be as steep as for a coastal site, but the variation of the wind resource may still be appreciable due to the large spatial extent of modern wind farms. Also, wind farm wakes propagate several kilometers downwind, adding complexity to the surrounding flow fields.[5,6] Under such conditions, power and wake assessments performed with analytical wake models are challenging due to the heterogeneity of the background velocity field. In fact, the local value of wind speed and turbulence intensity measured several hundreds of meters upstream of the farm are usually the only flow characteristics used by existing wake models.[7–10] The goal of the current study is to develop a new wake-merging method that accounts for a spatially varying background velocity and to further validate it against other wake-merging methods, numerical results and field measurements.

The Jensen model,[11] dating back to four decades ago, is one of the first ever analytical single-wake model. It states that

$$\frac{\Delta U(\boldsymbol{x})}{U_\mathrm{b}} = \frac{1-\sqrt{1-C_\mathrm{T}}}{(1+2\delta(x)/D)^2}\,\mathcal{H}\left(\frac{D}{2}+\delta(x)-r(\boldsymbol{x})\right) \tag{1}$$

where $\boldsymbol{x}=(x,y,z)$ with x the horizontal, y the lateral and z the vertical direction and $r(\boldsymbol{x})=(y^2+z^2)^{1/2}$ denotes the radial distance from the center of the wake. Moreover, U_b represents the background velocity, C_T is the wind-turbine thrust coefficient, $\delta(x)=k^*x$ is the wake width with k^* the wake expansion coefficient, D is the turbine rotor diameter, $\mathcal{H}$ denotes the Heaviside function and $\Delta U(\boldsymbol{x})=U_\mathrm{b}-U(\boldsymbol{x})$ is the velocity deficit in the wake, with $U(\boldsymbol{x})$ representing the waked velocity. Note that we are assuming the background velocity field to be uniform and uni-directional (i.e., only the horizontal component of the velocity field is non-zero). This model is derived applying only the mass conservation law in a control volume located downwind of the turbine.[12] Despite the lack of conservation of momentum, the Jensen model is one of the most used in both academic studies[13,14] and commercial software.[15,16] Later, Frandsen et al[17] proposed a new wake model based on both mass and momentum conservation laws applied on a control volume located around the turbine. Both the Jensen and Frandsen model assume a top-hat shape for the velocity deficit in the wake. This assumption leads to an underestimation of $\Delta U(\boldsymbol{x})$ at the center of the wake and to an overestimation of the velocity deficit at the edges. Since the power depends on the cube of the wind speed, the top-hat shape assumption can lead to large errors when used for predicting farm energy output.[10,12]

Bastankhah and Porté-Agel[12] have shown that the velocity deficit $\Delta U(\boldsymbol{x})$ collapses on to a Gaussian curve when plotted against the radial distance from the wake centerline, i.e. the wake of a turbine is self-similar.[18] Hence, they have written the normalized velocity deficit as

$$\frac{\Delta U(\boldsymbol{x})}{U_\mathrm{b}} = W(\boldsymbol{x}), \quad \text{with} \quad W(\boldsymbol{x}) = C(x) f(r(\boldsymbol{x}),\sigma(x)) \tag{2}$$

where $C(x)$ denotes the maximum normalized velocity deficit at each downwind location, $\sigma(x)$ represents a length scale which varies downstream and $f(r(\boldsymbol{x}),\sigma(x))$ describes the shape of the velocity profile. Equation (2) allows to solve analytically the mass and momentum equations. Moreover, in a self-similar state, the transverse distribution of the normalized mean velocity deficit remains Gaussian, which simplifies the wake modeling. While the shape function $f(r(\boldsymbol{x}),\sigma(x))$ is prescribed, the maximum normalized velocity deficit $C(x)$ is derived from the mass and momentum conservation laws.[12,19] The firsts three models displayed in Table 1 show three different $C(x)$ relations derived with distinct shape functions. The Gaussian wake model[12] assumes a Gaussian-like velocity deficit profile. It has proven to outperform both the Jensen and Frandsen model[12] and is nowadays widely used in wake assessments and layout optimization problems.[20,21] However, this model does not conserve momentum in the near-wake region, i.e. when $C_\mathrm{T} > 8\sigma^2/D^2$. To improve this deficiency, the super-Gaussian wake model uses a top-hat shape function in the near-wake region which evolves to a Gaussian shape in the far wake.[22,23] A different approach to improve the Gaussian wake model in the near-wake region is offered by the double-Gaussian wake model,[24,25] which includes the nacelle effects using two Gaussian functions which are symmetric with respect to the wake center. Results have shown that the double-Gaussian model outperforms the Gaussian model in the near-wake region, but it overestimates the velocity deficit far downstream of the turbine.[24] Other types of models prescribe the shape function

TABLE 1 Shape function $f(r(\boldsymbol{x}),\sigma(x))$ and maximum normalized velocity deficit $C(x)$ of four single-wake models

Model	$f(r,\sigma)$	$C(x)$ $(x > 0)$
Gaussian	$\exp\left(-\frac{r^2}{2\sigma^2}\right)$	$1-\sqrt{1-\frac{C_\mathrm{T}}{8(\sigma/D)^2}}$
Super-Gaussian	$\exp\left(-\frac{r^n}{2\sigma^2}D^{2-n}\right)$	$2^{2/n-1}-\sqrt{2^{4/n-2}-\frac{nC_\mathrm{T}}{16\Gamma(2/n)(\sigma/D)^{4/n}}}$
Double-Gaussian	$\frac{1}{2}\left[\exp\left(-\frac{(r+r_0)^2}{2\sigma^2}\right)+\exp\left(-\frac{(r-r_0)^2}{2\sigma^2}\right)\right]$	$\frac{M-\sqrt{M^2-1/2NC_\mathrm{T}D^2}}{2N}$
Ishihara	$\exp\left(-\frac{r^2}{2\sigma^2}\right)$	$\frac{1}{\left(a+bx/D+c(1+x/D)^{-2}\right)^2}$

Note: That $C(x)=0$ for $x \le 0$.

and derive the maximum velocity deficit $C(x)$ by fitting of numerical results and experimental data. The idea behind these data-driven models is to surgically insert error terms in the equations and further learn the associated parameters using operation data. The models proposed by Ishihara and Qian[26] and Schreiber et al.[27] are an example. In the current manuscript, we use the Ishihara and Qian[26] model, which is also reported in Table 1, and for brevity we denote it as the Ishihara model. Finally, note that when $f(r(\boldsymbol{x}),\sigma(x))$ is assumed to be Gaussian-like, the length scale $\sigma(x)$ represents the standard deviation of the Gaussian function.

The wake models mentioned above are used for wake assessments of single wind turbines. However, to estimate the power output of large farms, we have to deal with multiple wakes. Hence, superposition methods are applied to account for wake overlapping. To date, two main superposition methods have been explored, i.e. summing the velocity deficits[7,10] or summing the square of the velocity deficits.[8,9] These methods read as

$$U(\boldsymbol{x}) = U_\mathrm{b} - \sum_{k=1}^{N_t} u_k W_k(\boldsymbol{x}) \tag{3}$$

$$U(\boldsymbol{x}) = U_\mathrm{b} - \sqrt{\sum_{k=1}^{N_t} (u_k W_k(\boldsymbol{x}))^2} \tag{4}$$

where $U(\boldsymbol{x})$ is the horizontal component of the waked flow while u_k denotes the wind velocity averaged over the rotor disk of turbine k. The product $u_k W_k(\boldsymbol{x})$ corresponds to a velocity deficit (see Equation (2)); therefore, Equation (3) proposed by Niayifar and Porté-Agel[10] evaluates the velocity field within the farm using a linear superposition of velocity deficits while Equation (4) proposed by Voutsinas et al.[9] uses a superposition of energy deficits. The models proposed by Lissaman[7] and Katic et al.[8] also use Equations (3) and (4), respectively, to merge wakes with the additional assumption of $u_k = U_\mathrm{b}$, that is the mean wind speeds experienced by downwind turbines are equal to the farm inflow velocity. Figure 1 displays a three-dimensional representation of the velocity field within a staggered farm with streamwise and spanwise spacings of $S_x = S_y = 6D$. The Jensen model combined with Equation (4) is used in Figure 1 (top) while the Gaussian model coupled with Equation (3) is adopted in Figure 1 (bottom). The plots reveal that a lower velocity gradient at the edges of the wakes is obtained with a Gaussian-like shape function, resulting in a better representation of reality. A more extensive comparison between the two models is performed in Section 4.

Very recently, a few wake engineering models have been proposed that account for a spatially varying background velocity field. The model of Brogna et al.[28] superimposes a Gaussian shape wake model on top of the background flow field. Farrell et al.[29] recently developed a model

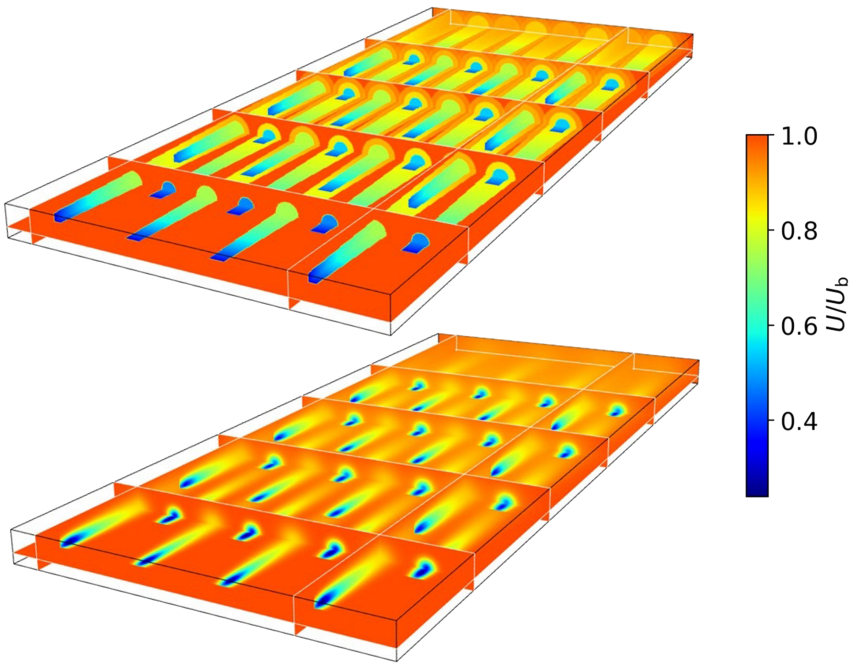

FIGURE 1 Normalized velocity field through a staggered farm with 32 turbines with rotor diameter $D = 154$ m, thrust coefficient $C_\mathrm{T} = 0.85$, ambient turbulence intensity $\mathrm{TI}_\mathrm{b} = 12\%$ and background velocity $U_\mathrm{b} = 10$ m/s. The dimensionless streamwise and spanwise spacings are $S_x = S_y = 6D$. (top) Jensen model combined with superposition of energy deficits and (bottom) Gaussian model coupled with linear superposition of velocity deficits

which evaluates the background flow velocity at turbine location using a Delaunay triangulation in combination with a barycentric interpolation and accounts for varying wind directions by rotating the numerical grid. However, both models use an adapted version of the sum-of-squares method proposed by Katic et al.[8] to merge wakes, which is based on empirical relations. Further, the model proposed by Shamsoddin and Porté-Agel[30] also accounts for varying background velocity. However, this model deals with the wake of a single turbine and it has never been extended to a farm level. In the current manuscript, we aim to fill the aforementioned gap by developing a new wake-merging method that accounts for spatial heterogeneity in the background flow field. The manuscript is structured as follows. First, Section 2 introduces the new wake-merging method and shows some of its features. Next, Section 3 describes the single-wake models setup and details the simulation cases. Thereafter, we compare the performance of the new wake-merging method against LES results, dual-Doppler radar measurements and SCADA data in Section 4. Finally, conclusions and suggestions for future research are drawn in Section 5.

2 | NEW WAKE-MERGING METHOD

In Section 2.1, we derive the new wake-merging method for a uni-directional flow which changes in magnitude along the streamwise and spanwise directions. Thereafter, in Section 2.2, we generalize the model considering a background velocity field which changes in direction over the wind farm area. Finally, some example cases which highlight the features of the new model are illustrated in Section 2.3.

2.1 | Uni-directional flow

Consider a wind-farm with N_t turbines displayed with an arbitrary layout. The turbines operate in a heterogeneous uni-directional background velocity field which we denote with $U_b(\boldsymbol{x})$. Moreover, the turbines are ordered according to the wind direction. To do so, we compute the point-line distance between the turbine coordinates and a line orthogonal to the wind direction upstream of the farm, and we sort the turbines from nearest to farthest. Next, to define the wake function $W_k(\boldsymbol{x})$, we introduce a new coordinate system $\boldsymbol{X}_k(\boldsymbol{x}) = (X_k(\boldsymbol{x}), Y_k(\boldsymbol{x}), Z_k(\boldsymbol{x}))$ per turbine which has its origin at turbine k, with location $\boldsymbol{x}_k = (x_k, y_k, z_{h,k})$, where $z_{h,k}$ is the turbine hub-height. We then express $W_k(\boldsymbol{x}) = \widehat{W}(\boldsymbol{X}_k(\boldsymbol{x}))$ where

$$X_k(\boldsymbol{x}) = x - x_k \tag{5}$$

$$Y_k(\boldsymbol{x}) = y - y_k \tag{6}$$

$$Z_k(\boldsymbol{x}) = z - z_{h,k} \tag{7}$$

with

$$\widehat{W}(\boldsymbol{X}_k) = C(X_k) f(r(\boldsymbol{X}_k), \sigma(X_k)). \tag{8}$$

Note that the maximum normalized velocity deficit and the wake width assume non-zero values only for $X_k(\boldsymbol{x}) > 0$.

To compute the flow through the farm, we use a recursive formula. The velocity field at the first iteration is given by the background wind speed, which is a model input. Hence, $U_0(\boldsymbol{x}) = U_b(\boldsymbol{x})$. Using self-similarity in the wake of the most upwind turbine (i.e., Equation (2)), we can write the velocity field $U_1(\boldsymbol{x})$ as

$$\frac{U_0(\boldsymbol{x}) - U_1(\boldsymbol{x})}{U_0(\boldsymbol{x})} = W_1(\boldsymbol{x}) \quad \Rightarrow \quad U_1(\boldsymbol{x}) = U_0(\boldsymbol{x})[1 - W_1(\boldsymbol{x})]. \tag{9}$$

More generally, given the flow field generated by the background field and the firsts $k-1$ turbines, the effect of the next turbine (k) is also expressed using self-similarity of the wake (of turbine k), so that

$$\frac{U_{k-1}(\boldsymbol{x}) - U_k(\boldsymbol{x})}{U_{k-1}(\boldsymbol{x})} = W_k(\boldsymbol{x}) \quad \Rightarrow \quad U_k(\boldsymbol{x}) = U_{k-1}(\boldsymbol{x})[1 - W_k(\boldsymbol{x})], \tag{10}$$

providing the general recursive formula for any value of k. Note that, if we define $\Delta U_k(\boldsymbol{x}) = U_{k-1}(\boldsymbol{x}) - U_k(\boldsymbol{x})$, Equation (10) becomes equivalent to Equation (2), where the background velocity is now $U_{k-1}(\boldsymbol{x})$. Finally, the full flow field in the farm (i.e. including the background flow and the

turbine wakes) is given by $U(\boldsymbol{x}) = U_{N_t}(\boldsymbol{x})$. For the current case of uni-directional flow, the recursive relation (Equation (10)) can be explicitly elaborated into

$$U(\boldsymbol{x}) = U_{\mathrm{b}}(\boldsymbol{x}) \prod_{k=1}^{N_t} [1 - W_k(\boldsymbol{x})], \quad \text{with} \quad W_k(\boldsymbol{x}) = \hat{W}(\boldsymbol{X}_k(\boldsymbol{x})). \tag{11}$$

Note that turbines downwind do not affect turbines located upwind. In fact, the wake function $W_k(\boldsymbol{x})$ is defined in such a way that $W_k(\boldsymbol{x}) = 0$ for any location $\boldsymbol{x}$ upstream of turbine k.

2.2 | Multi-directional flow

We now generalize the ideas discussed above for multi-directional flow. To this end, we consider an arbitrary farm layout now immersed in a heterogeneous background velocity field which changes direction and magnitude throughout the farm. Hence, $\boldsymbol{U}_{\mathrm{b}}(\boldsymbol{x}) = (U_{\mathrm{b}}(\boldsymbol{x}), V_{\mathrm{b}}(\boldsymbol{x}))$, and $\theta_{\mathrm{b}}(x,y) = \arctan(V_{\mathrm{b}}(\boldsymbol{x})/U_{\mathrm{b}}(\boldsymbol{x}))$ defines the local orientation of the background flow. For sake of simplicity, we keep the turbines aligned with the flow (i.e., no yaw misalignment). We also assume that the vertical velocity component of the background velocity field is zero and that the background flow does not change direction along the z axis, meaning that the ratio $V_{\mathrm{b}}(\boldsymbol{x})/U_{\mathrm{b}}(\boldsymbol{x})$ is constant with height. Finally, we presume that the wakes in the farm are carried by the background flow $\boldsymbol{U}_{\mathrm{b}}(\boldsymbol{x})$. Thus, the coordinate system $\boldsymbol{X}_k(\boldsymbol{x}) = (X_k(\boldsymbol{x}), Y_k(\boldsymbol{x}), Z_k(\boldsymbol{x}))$ still has origin at the turbine location (i.e., $\boldsymbol{X}_k(\boldsymbol{x}_k) = \boldsymbol{0}$) but is now oriented along the streamlines of the background flow field. Hence,

$$X_k(\boldsymbol{x}) = \int_{x_k}^{x} \cos(\theta_{\mathrm{b}}(\bar{x}, y))d\bar{x} + \int_{y_k}^{y} \sin(\theta_{\mathrm{b}}(x, \bar{y}))d\bar{y} \tag{12}$$

$$Y_k(\boldsymbol{x}) = -\int_{x_k}^{x} \sin(\theta_{\mathrm{b}}(\bar{x}, y))d\bar{x} + \int_{y_k}^{y} \cos(\theta_{\mathrm{b}}(x, \bar{y}))d\bar{y} \tag{13}$$

$$Z_k(\boldsymbol{x}) = z - z_{\mathrm{h},k}. \tag{14}$$

Next, we construct the recursive formula. To this end, we first order the turbines from most upstream to most downstream, so that for any $k > l$, the wake of turbine k does not interfere with turbine l. This can be achieved by using the same technique adopted for uni-directional flows, but now the sorting algorithm has to be built by computing the point-line distance along the curvilinear system which follows the streamlines of the background flow, and where the upstream line (curve) is constructed to be locally orthogonal to the streamlines. The starting term of the recursion is given again by $\boldsymbol{U}_0(\boldsymbol{x}) = \boldsymbol{U}_{\mathrm{b}}(\boldsymbol{x})$, but the recursive formula now becomes

$$\boldsymbol{U}_k(\boldsymbol{x}) = (\boldsymbol{U}_{k-1}(\boldsymbol{x}) \cdot \boldsymbol{e}_{\perp,\mathrm{k}})(1 - W_k(\boldsymbol{x}))\boldsymbol{e}_{\perp,\mathrm{k}} + (\boldsymbol{U}_{k-1}(\boldsymbol{x}) \cdot \boldsymbol{e}_{\|,k})\boldsymbol{e}_{\|,k}, \quad \text{for } k = 1, \ldots, N_t \tag{15}$$

with the total farm flow field given by $\boldsymbol{U}(\boldsymbol{x}) = \boldsymbol{U}_{N_t}(\boldsymbol{x})$ and $W_k(\boldsymbol{x}) = \widehat{W}(\boldsymbol{X}_k(\boldsymbol{x}))$. Moreover, $\boldsymbol{e}_{\perp,\mathrm{k}} = (\cos\theta_k, \sin\theta_k)$ and $\boldsymbol{e}_{\|,k} = (-\sin\theta_k, \cos\theta_k)$ denote the unit vector perpendicular and parallel to the rotor plane of turbine k with θ_k the turbine orientation angle (defined below). Equation (15) simply expresses that the wake deficit is oriented in the axial direction of turbine k, while no velocity change occurs in the parallel direction. This axial velocity deficit is then transported along the streamlines of the background flow as expressed by the coordinate system $\boldsymbol{X}_k(\boldsymbol{x})$. Finally, the angle θ_k which corresponds to the orientation of turbine k is defined as

$$\theta_k \triangleq \arctan(V(\boldsymbol{x}_k)/U(\boldsymbol{x}_k)) = \arctan(V_{k-1}(\boldsymbol{x}_k)/U_{k-1}(\boldsymbol{x}_k)), \tag{16}$$

where the second equality follows from the ordering of the turbines.

Note that we have used the simplifying assumption that the coordinate system $\boldsymbol{X}_k(\boldsymbol{x})$ (Equations (12)–(14)) is oriented along the background flow. This can be further generalized so that $\boldsymbol{X}_k(\boldsymbol{x})$ is oriented along the streamlines of the full flow $\boldsymbol{U}(\boldsymbol{x})$. However, this would require an iterative procedure, that is starting with orientation along the background flow as an initial guess, and then iteratively updating the streamlines using Equations 12–16 (e.g., based on a Newton method or a fixed-point iteration method). This is not further considered here and it is work for future research.

Equation (15) can also be further generalized to include effects of yaw misalignment. In such case, the orientation of turbine k would be expressed as $\tilde{\theta}_k = \theta_k + \gamma_k$ with γ_k the yaw angle of turbine k. Moreover, the wake deficit function would need to be extended to include yaw effects (see, e.g., Bastankhah and Porté-Agel[31] and Qian and Ishihara[32]). However, the effects of yaw misalignment will be investigated in the future and are not included in the current manuscript.

In the discussion above, the wake function $W(\boldsymbol{x})$ can be selected from Table 1. However, the derivation of $C(x)$ assumes that the background velocity field upstream of the turbine is uniform in the stream and cross-stream directions.[12,19] Instead, in our derivation the background velocity perceived by the turbine k is non-uniform due to heterogeneity in the background velocity field and preceding wakes. Hence, the maximum normalized velocity deficit proposed by Shamsoddin and Porté-Agel[30] should be adopted. However, the assumptions of slow varying background velocity in the horizontal directions and large enough turbine spacings allow us to obtain the same functions $C(x)$ reported in Table 1 (i.e., assuming that the x and y derivative of both components of $\boldsymbol{U}_{k-1}(\boldsymbol{x})$ at location $\boldsymbol{x}_k$ are negligible). In other words, Equation (15) conserves mass and momentum only if the waked flow induced by preceding turbines at the location of a downwind turbine is quasi-homogeneous in the horizontal directions and if a slow varying background velocity is used. Note that this is usually the case for velocity changes induced by coastal gradients. For example, Barthelmie et al[1] observed an average wind speed difference of 0.1 m/s between nearest and farthest turbine from the shore for the Horns Rev farm.

Next, the inflow velocity of turbine k is obtained by averaging the velocity over the turbine rotor disk. To this end, we use a quadrature rule with $N_q = 16$ points spread over the rotor swept area. The quadrature-point coordinates are denoted with $\boldsymbol{x}_{k,q}$ and are chosen following the quadrature rule proposed by Holoborodko[33] with uniform weighting factor $\omega_q = 1/N_q$. Hence

$$u_k = \sum_{q=1}^{N_q} \omega_q S(\boldsymbol{x}_{k,q}) \tag{17}$$

where $S(\boldsymbol{x}) = \|\boldsymbol{U}(\boldsymbol{x})\|_2$. We also refer to Allaerts and Meyers[34] for more details on the quadrature rule. The turbine power is then obtained from $P_k = P_c^k(u_k)$ where P_c^k denotes the power curve of turbine k. Similarly, the turbine set-point is computed as $C_{T,k} = C_{T,c}^k(u_k)$, where $C_{T,c}^k$ is the thrust coefficient curve of turbine k. Finally, to compute the turbulence intensity within the farm, we adopt the model proposed by Niayifar and Porté-Agel[10] which expresses $TI = \left(TI_b^2 + TI_+^2\right)^{1/2}$ where TI_b denotes the ambient turbulence intensity while TI_+ represents the added turbulence intensity generated by a wind turbine. The added turbulence intensity is computed with the model of Crespo and Hernandez.[35] Note that we are assuming TI_b to be uniform in and around the wind farm.

2.3 | Example cases

To illustrate some features of the new wake-merging method, we report a couple of simple examples here. The background velocity $\boldsymbol{U}_b(\boldsymbol{x})$ is a model input. For instance, $U_b(\boldsymbol{x})$ and $V_b(\boldsymbol{x})$ could be three-dimensional fields taken in the vicinity of an operating farm (see Nygaard and Newcombe[36] and Djath et al.[5]) or, ideally, the velocity fields which would manifest assuming that the farm would not operate. If measurements are not available, the background velocity needs to be modeled.

In a first application, we consider a uni-directional horizontally homogeneous background velocity field with a logarithmic profile[37] in the vertical direction (i.e., $U_b = U_b(z)$), with friction velocity and surface roughness of 0.58 m/s and 0.1 m, respectively. These values lead to a wind speed at $z_h = 120$ m of 10 m/s. Moreover, the ambient turbulence intensity is fixed to $TI_b = 12\%$. A row of five turbines with streamwise spacing of $S_x = 7D$ is immersed in such atmospheric conditions, with $D = 154$ m. Figure 2 shows a side view of the velocity field through the row of turbines obtained with the new wake-merging method coupled with the Gaussian wake model. The wake expansion in the vertical direction mimics the formation of an internal boundary layer[38,39] which grows along the streamwise direction. Moreover, the maximum normalized velocity deficit decreases monotonically in the wake of each turbine, resulting in a velocity recovery. Note that the Gaussian wake model does not conserve momentum in the near-wake region, that is, when $C_T > 8\sigma^2/D^2$ (see Table 1)—we fix $C_T = 0.85$ here. To represent the velocity deficits in this region, the thrust coefficient is written as an error function of the streamwise coordinate, similarly to Zong and Porté-Agel.[40] Finally, note that ground-wake interactions are neglected throughout the whole manuscript. In fact, the image method inherently assumes a slip boundary

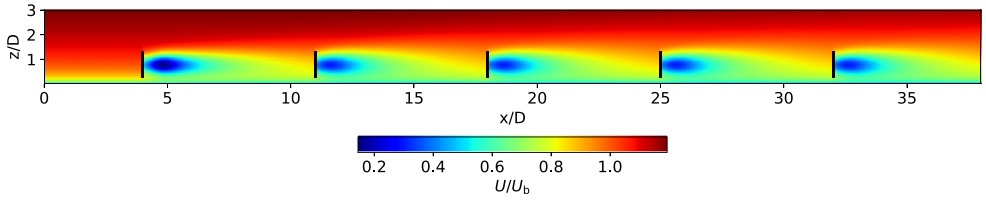

FIGURE 2 Side view of the normalized velocity field at the turbine centerline plane for a single row of five turbines with streamwise spacing of $S_x = 7D$. The velocity field is computed with the new wake-merging method coupled with the Gaussian wake model. The velocity U_b is homogenous in the x and y direction. The black lines denote the wind-turbine rotor locations

condition which could cause issues when logarithmic shear profiles or mesoscale velocity fields are used as a model input, since in these cases the ground surface is not a symmetry plane.

As a second application, we consider a farm of 25 turbines immersed in a multi-directional spatially varying background velocity field. More specifically, Figure 3A,B illustrates the turbines' wake behavior in presence of a gradual change in background velocity magnitude along the streamwise and spanwise directions, respectively (i.e., the background wind speed increases linearly along the streamwise (spanwise) direction with a difference of 2 m/s between $x/D = 0$ ($y/D = 0$) and $x/D = 50$ ($y/D = 40$)). Thereafter, Figure 3C shows the flow through a farm which is subject to a gradual change in wind direction. In this specific case, we assume $S_b = \|\boldsymbol{U}_b(\boldsymbol{x})\|_2 = 10$ m/s and we vary the wind direction with $\theta_b(x) = 0.35x/D$, so that there is a 10° change in background wind direction between the first and the last column of turbines.

In the current section, we have shown that the proposed wake-merging method properly accounts for preceding wakes. Moreover, the new method does not rely on a single velocity value taken upstream of the farm. Instead, the turbine wakes are superimposed on heterogeneous background velocity fields. Despite the added features, the computation of the velocity through a farm is done within seconds, making the model suitable for optimization studies and annual energy yield assessments. A more extensive validation is performed in Section 4, where we compare the model's performance against numerical results and field measurements in homogeneous and heterogeneous conditions. Moreover, more insights about the differences between the new and the linear superposition method are provided in Appendix A.

3 | CASES DESCRIPTION AND SINGLE-WAKE MODEL SETUP

In this manuscript, we compare the performance of nine engineering wake models: the Gaussian[12] (G), super-Gaussian[23] (SG), double-Gaussian[24] (DG) and Ishihara[26] (I) single-wake models coupled with linear superposition of velocity deficits (Lin—Equation (3)) and with our new wake-merging method (New—Equation (15)). As an additional reference, we also show results from the Jensen model[11] combined with quadratic superposition (Equation (4)). In the remainder of this section, we will briefly describe the setup of the aforementioned single-wake models. For sake of simplicity, we assume uni-directional flow with the stand-alone turbine located in position $x_1 = y_1 = 0$, so that no horizontal axes transformation is needed.

The Jensen model, which we use as a standard reference in the current work, evaluates the normalized velocity deficit using Equation (1), which depends on the wake expansion coefficient k^*, the only free parameter. Jensen[11] assumed $k^* = 0.1$. Further offshore wind-farm studies

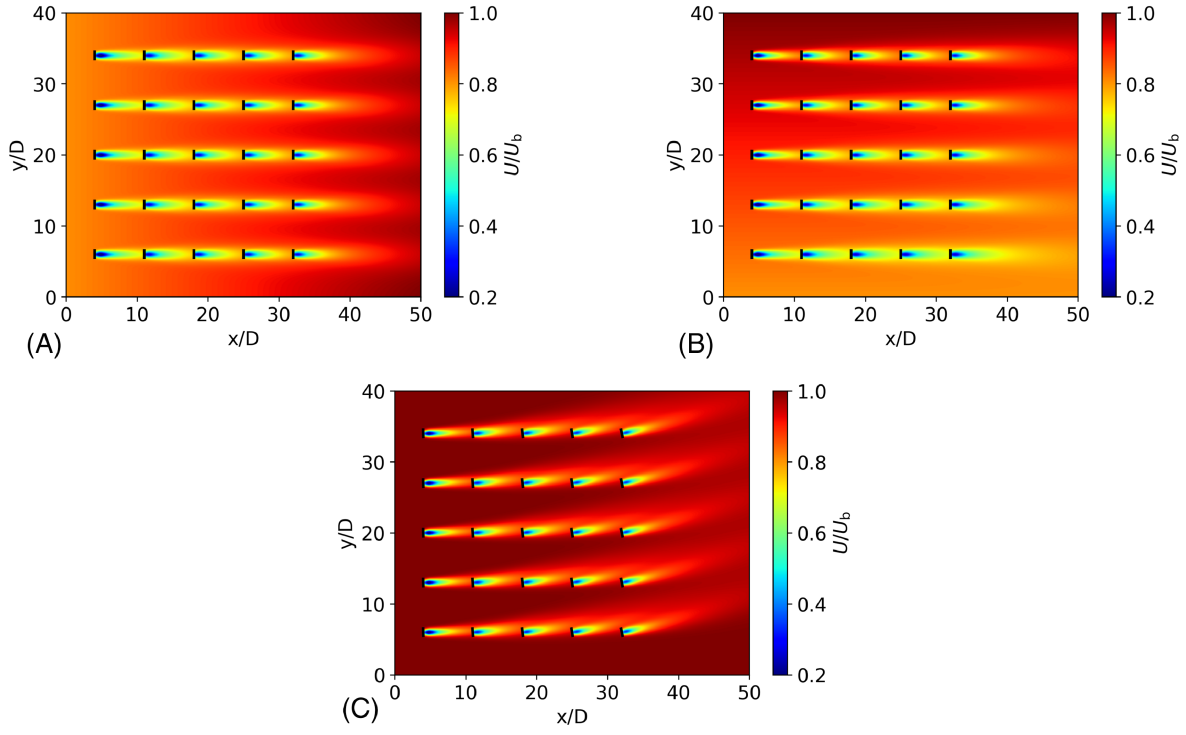

FIGURE 3 Top view of the normalized velocity field at a horizontal plane at hub height computed with the new wake-merging method coupled with the Gaussian wake model. (A,B) Gradual change of background velocity magnitude along the streamwise and spanwise directions, respectively. (C) Gradual change of background velocity direction over the wind farm. The farm contains 25 turbines with dimensionless streamwise and spanwise spacing of $S_x = S_y = 7D$, respectively. The black lines denote the wind-turbine rotor locations

noted that a smaller wake expansion coefficient enhances the model's performance.[36,41–43] Hence, the value $k^* = 0.04$ is typically used nowadays. Moreover, very recently, k^* has been expressed as function of the turbulence intensity, which could further improve the model's predictions.[14,44,45] In the current study, we assume $k^* = 0.04$.

The Gaussian wake model used in our analysis is the one proposed by Bastankhan and Porté-Agel.[12] The shape function and parameter $C(x)$ are reported in Table 1. Similarly to Jensen,[11] a linear expansion of the Gaussian profile standard deviation, and consequently also of the wake width, is assumed, that is,

$$\sigma(x) = k^* x + \varepsilon D \tag{18}$$

where $\varepsilon = 0.2\sqrt{\beta}$ is the limit value of $\sigma(x)/D$ for x approaching 0, with

$$\beta = \frac{1}{2}\frac{1+\sqrt{1-C_T}}{\sqrt{1-C_T}}. \tag{19}$$

Contrary to the Jensen model, the wake expansion coefficient is expressed as a function of the turbulence intensity following the empirical relation proposed by Niayifar and Porté-Agel,[10] that is $k^* = 0.3837\,TI + 0.003678$. Note that this empirical relation provides good estimates of k^* for turbulence intensity values in the range of $0.065 < TI < 0.15$.

The choice of a super-Gaussian shape function implies a n-dependent maximum normalized velocity deficit $C(x)$ (see Table 1). For high values of n, the shape function resembles a top-hat filter, while for low values the function evolves toward a Gaussian shape. If $n = 2$, the model is identical to the Gaussian one. Blondel and Cathelain[23] proposed the following expression for the order $n(x)$

$$n(x) = a_f e^{b_f x/D} + c_f. \tag{20}$$

Regarding the standard deviation of the Gaussian profile, the following linear form is used

$$\sigma(x) = [a_s TI + b_s]x + c_s\sqrt{\beta}D. \tag{21}$$

Blondel and Cathelain [23] proposed a first calibration of the model with parameters not dependent on the thrust coefficient and turbulence intensity values. However, in a later study, Cathelain et al [46] re-calibrated the model by minimizing the difference between predictions and LES results using a larger weight on the error in the near-wake than in the far-wake region. In the current manuscript, we use the latter calibration. Hence, $a_s = 0.18$, $b_s = 0.0119$, $c_s = 0.0564C_T + 0.13$, $b_f = 1.59\exp(-23.31TI) - 2.15$ and $c_f = 2.98$. Finally, a_f is derived by imposing $C(0) = a$, with $a = 1/2\left(1-\sqrt{1-C_T}\right)$ the axial induction factor. To compute a_f, we have used the bisection method provided in the SciPy library.[47] Note that with the current parameter selection, the super-Gaussian wake model does not converge to the Gaussian one in the far-wake region. We refer to the original publication for more details.[23]

In an attempt to improve the Gaussian wake model in the near-wake region, a double-Gaussian model was first proposed by Keane et al.[25] and further corrected and re-calibrated by Schreiber et al.[24] In this model, the shape function is assumed to have a double-Gaussian profile. Moreover, the parameter $C(x)$ (see Table 1) depends upon two analytically derived functions

$$M(x) = 2\sigma^2(x)\exp\left(-\frac{r_0^2}{2\sigma^2(x)}\right) + \sqrt{2\pi}r_0\sigma(x)\,\mathrm{erf}\left(\frac{r_0}{\sqrt{2}\sigma(x)}\right) \tag{22}$$

$$N(x) = \sigma^2(x)\exp\left(-\frac{r_0^2}{\sigma^2(x)}\right) + \frac{\sqrt{\pi}}{2}r_0\sigma(x)\,\mathrm{erf}\left(\frac{r_0}{\sigma(x)}\right) \tag{23}$$

where $r_0 = Dk_r/2$ represents the radial position of the Gaussian extrema. Following Schreiber et al,[24] we set $k_r = 0.535$ in the current manuscript. The standard deviation of the Gaussian profile used by Schreiber et al[24] reads as

$$\sigma(x) = k^*(x - s_0) + \varepsilon D \tag{24}$$

with $s_0 = 4.55D$ the stream tube outlet position. However, we have noticed that this parametrization of the standard deviation leads to a strong overestimation of the velocity deficits in the far-wake region, causing unrealistic power loss predictions when the model is coupled with superposition methods (not shown). To avoid this issue, we have fixed $s_0 = 1.5D$. Moreover, the model admits momentum conserving solutions only if $M^2(x) - 1/2N(x)C_TD^2 \geq 0$, which does not occur for large C_T values and low ambient turbulence intensity. For further details, we refer to the publication of Schreiber et al.[24]

The only data-driven model considered in our analysis is the one proposed by Ishihara and Qian.[26] This model assumes a Gaussian shape function and it uses a parameter $C(x)$ defined as

$$C(x) = \frac{1}{\left(a + bx/D + c(1 + x/D)^{-2}\right)^2} \tag{25}$$

with

$$a = 0.93 C_T^{-0.75} TI^{0.17}, \tag{26}$$

$$b = 0.42 C_T^{0.6} TI^{0.2}, \tag{27}$$

$$c = 0.15 C_T^{-0.25} TI^{-0.7}. \tag{28}$$

The expressions of these parameters are derived from fitting of numerical results and wind tunnel experiments (see Ishihara and Qian[26] for more information).

Velocity fields at a horizontal plane at hub height for a stand-alone wind turbine computed with the five single-wake models described above are illustrated in Figure 4. The thrust set-point of the turbine is $C_T = 0.7$ with $D = 154$ m. The ambient turbulence intensity is $TI_b = 12\%$ and a homogeneous uni-directional background velocity field of 10 m/s is used. It is worth to notice that the ratio U/U_b predicted by the Jensen and super-Gaussian wake models is close to 0.9 at $15D$ downstream of the turbine (see Figures 4A and C, respectively), which is low if compared with results of the other single-wake models. Moreover, the Gaussian, double-Gaussian and Ishihara models predict a similar wake profile far downstream the turbine and differ only in the near-wake region (i.e., when $x/D < 5$). Note that the Gaussian model does not conserve momentum when $C_T > 8\sigma^2/D^2$ (which corresponds to $x/D < 3/2$ in the current example). The thrust coefficient is written as an error function of the streamwise coordinate to simulate the wake deficits in this region (see Zong and Porté-Agel[40]).

In the remainder of the manuscript, the eight wake engineering models used in our analysis are denoted with Lin–G, Lin–SG, Lin–DG, Lin–I, New–G, New–SG, New–DG, New–I, where the first acronym specifies the superposition method, the hyphen has to be read as "coupled with" and the second acronym identifies the single-wake model. Moreover, the Jensen model coupled with quadratic superposition is simply denoted with "Jensen". All wind-farm models with a turbulence-dependent wake decay coefficient use the method proposed by Niayifar and Porté-Agel[10] (which is inspired by the work of Frandsen and Thøgersen[48]) for computing the turbulence intensity through the farm. The performance of the nine wind-farm models mentioned above is compared against numerical results, dual-Doppler radar measurements and Supervisory Control and Data Access (SCADA) data for three different wind farms, namely the Horns Rev, London Array and Westermost Rough. The farms characteristics are reported in Table 2. Moreover, Figure 5 shows the thrust and power curves of the turbines installed in the farms. The power and the thrust coefficient of a generic turbine k are evaluated as $P_k = P_c^k(u_k)$ and $C_{T,k} = C_{T,c}^k(u_k)$, respectively. The results of our analysis are shown in the next section.

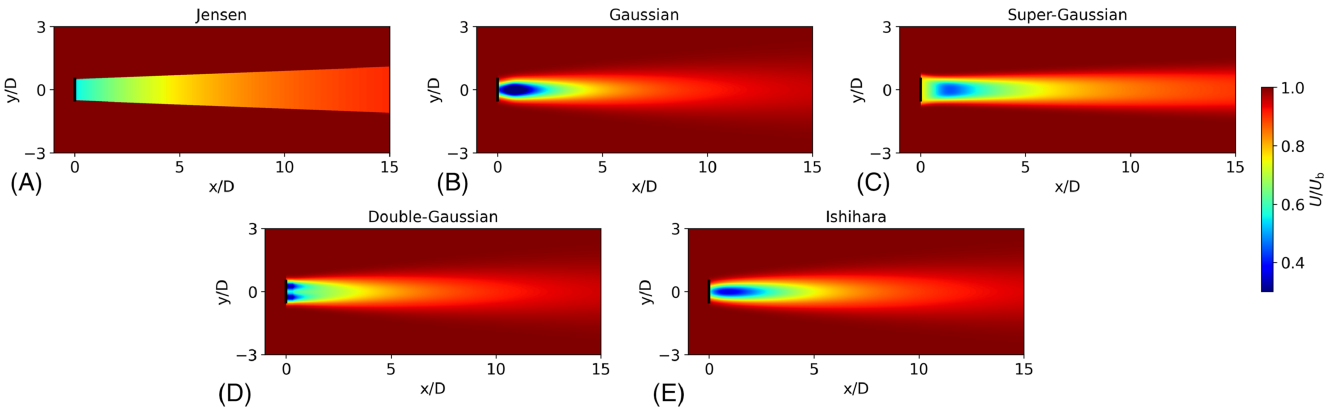

FIGURE 4 Top view of the normalized velocity field at a horizontal plane at hub height computed with the (A) Jensen, (B) Gaussian, (C) super-Gaussian, (D) double-Gaussian and (E) Ishihara single-wake model. The black lines denote the wind-turbine rotor locations

TABLE 2 Farms characteristics and types of data used

Wind farm	Capacity [MW]	N° of turbines	Hub height [m]	Rotor diameter [m]	Turbine	Data
Horns Rev	160	80	70	80	Vestas V-80	LES, SCADA
London Array	630	175	84.5	120	SWT-120-3.6	SCADA
Westermost Rough	210	35	106	154	SWT-154-6.0	Dual-Doppler radar

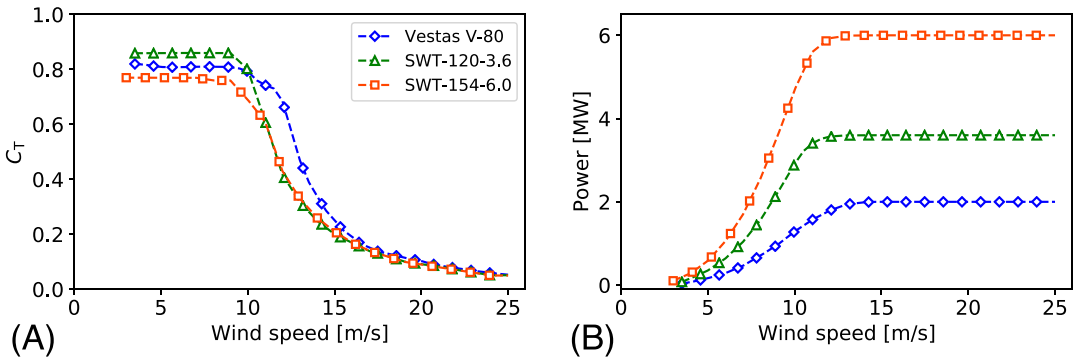

FIGURE 5 (A,B) Thrust and power curves of the Vestas V-80, SWT-120-3.6 and SWT-154-6.0 wind turbines. The thrust curve of the Vestas V-80 is provided by Wu and Porté-Agel[49] while the power curve is available at The-Wind-Power.com.[50] The thrust curve of the SWT-120-3.6 turbine is available at wind-turbine-models.com[51] while the power curve is accessible at The-Wind-Power.com.[52] The SWT-154-6.0 turbine thrust and power curves are available at Commissiemer.nl[53]

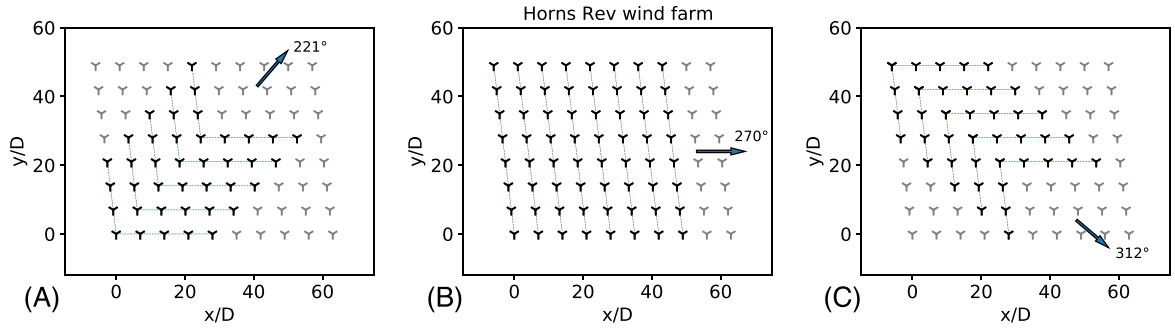

FIGURE 6 Layout of the Horns Rev farm with distances normalized by the rotor diameter. The SCADA data are averaged along the dotted green lines and are only available for turbines marked in black for three wind sectors (±5°, ±10° and ±15°) centered on wind directions of (A) 221°, (B) 270°, and (C) 312°

4 | RESULTS AND DISCUSSION

The aim of this section is to compare the performance of the linear superposition method introduced by Niayifar and Porté-Agel[10] with the new wake-merging method when coupled with different single-wake models. As an additional reference, we also include the Jensen model in the analysis. The power predictions are compared against LES results and SCADA data from the Horns Rev and London Array wind farms in Section 4.1 and 4.2, respectively. In such cases, a homogeneous background velocity field is used. On the other hand, we compare the models' performance in heterogeneous conditions in Section 4.3, where the background velocity field is reconstructed from dual-Doppler radar measurements taken at the Westermost Rough farm. Note that we assume a vertically homogeneous background flow with constant wind direction in all cases.

4.1 | Horns Rev

Horns Rev was the first offshore wind farm in the North Sea, located 15 km off the westernmost point of Denmark. Eighty Vestas V-80 are laid out as an oblique rectangle with a streamwise and spanwise spacings of 7*D*. The farm layout is shown in Figure 6 while the farm characteristics are detailed in Table 2. The thrust curve of the Vestas V-80 is provided by Wu and Porté-Agel[49] while the power curve is, for example, available at The-Wind-Power.com[50] and are both shown in Figure 5.

First, we compare the farm power output predicted by the models with LES results. Following Porté-Agel et al,[54] we set the background velocity to 8 m/s, with ambient turbulence intensity of 7.7% (see Porté-Agel et al[54] and Niayifar and Porté-Agel[10] for more details on the LES setup). Figure 7A illustrates the Horns Rev power output as function of the wind direction (from 173° to 353°). Note that the power is normalized by the wake-less power (i.e. the power that the farm would extract if all turbines would operate as front-row turbines). To better summarize the models' performance, Figure 7B displays the distribution of the difference between model (P^{wf}_{Model}) and LES (P^{wf}_{LES}) farm power output across all wind directions normalized by the wake-less power, which is computed as

$$\Delta_{M-L} = \frac{P^{wf}_{Model} - P^{wf}_{LES}}{N_t P_1} \tag{29}$$

where N_t is the total number of wind turbines and $P_1 = P_c(U_b) = 0.701$ MW is the power extracted by a stand-alone turbine. To put things into perspective, a Δ_{M-L} of 10% corresponds to a difference in farm power output between model and LES results of 5.6 MW (3.5% of the farm rated power). Note that positive values of Δ_{M-L} denote an overestimation of farm power output. Overall, the new wake-merging method performs similarly to linear superposition. In fact, when combining the predictions of all single-wake models, the mean absolute error (MAE) between predictions and LES results computed with the linear and new wake-merging methods are of 3.6% and 4%, respectively. The higher MAE obtained with the new wake-merging method is due to a slightly higher power underestimation occurring for low turbine spacing values (i.e., for wind directions of 221°, 270° and 312°). Both the Gaussian and double-Gaussian wake models show very accurate power predictions with MAEs of 2.4% and a maximum power underestimation of about 7%, which occurs at 270° On the other hand, the Jensen and super-Gaussian wake models show negative biases and wider interquartile ranges (IQRs), performing poorly when the farm is exposed to wind directions for which there is a small streamwise distance between turbines (see Figure 7A). The bad performance obtained with the super-Gaussian model could be attributed to a sub-optimal choice of the tuning parameters. In fact, the choice of $c_f = 2.98$ leads to higher velocity deficits in the far-wake region with respect to the Gaussian wake model, as shown in Figure 4B,C. Finally, the Ishihara model mainly overestimates the power output, with a MAE of 4.8%. Note that the Jensen model is the only one that uses a top-hat shape function, which explains the staircase (and less realistic) power behavior observed in Figure 7A.

Next, we compare the models' performance with SCADA data taken from Barthelmie et al.[55] These data were recorded at a wind speed of 8 ±0.5 m/s with 7.7% ambient turbulence intensity and consist in power ratios averaged over three wind sectors (i.e., ± 5°, ± 10° and ± 15°) centered on three mean wind directions (i.e., 221°, 270°, and 312°). The power ratios are available only for turbines labeled in black in Figure 6 and

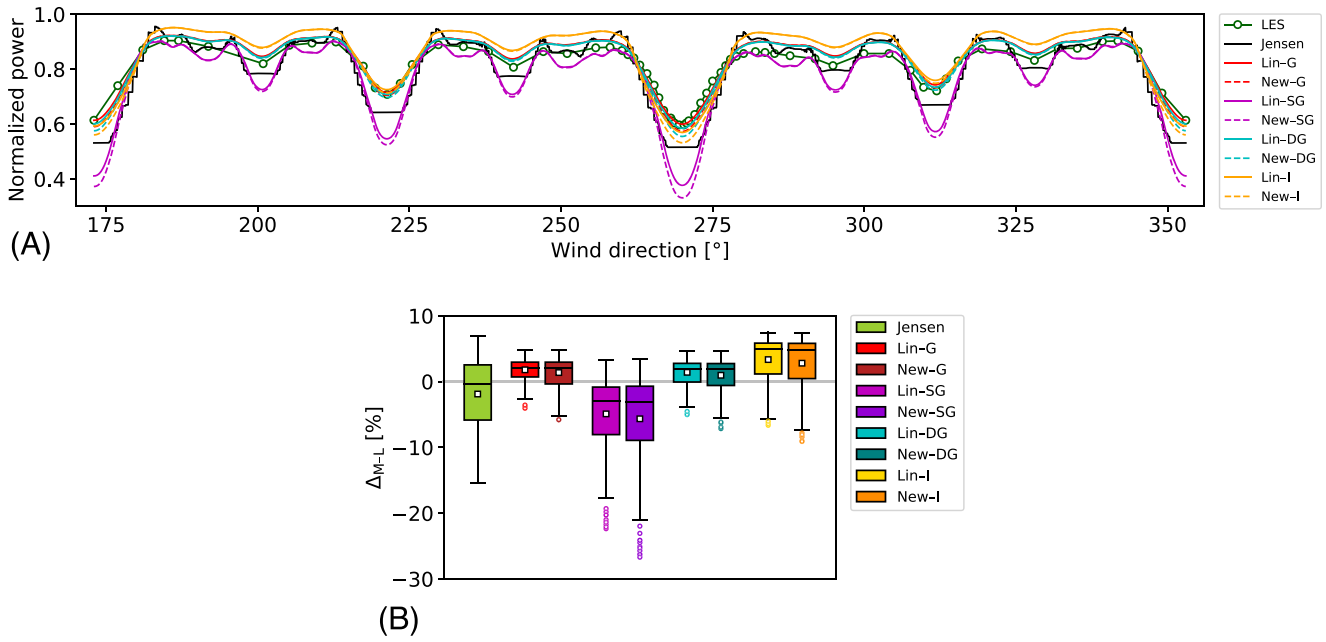

FIGURE 7 (A) Horns Rev power output computed with LES and nine analytical wind-farm models normalized by the wake-less power and expressed as function of the wind direction. (B) Distribution of the difference in farm power output between analytical models and LES across all wind directions normalized by the wake-less power. The box bounds the interquartile range (IQR). The horizontal black line and the white square denote the median and the mean, respectively. The whiskers extend to a maximum of 1.5×IQR beyond the box. The dots represent outliers

are averaged along the dotted green lines. Figure 8 illustrates the modeled and observed power ratios for the three transects. These ratios are averaged over the studied sector using 1° increments and are further averaged over the wind speed range 8 ± 0.5 m/s using increments of 0.5 m/s. Overall, the observations show lower power ratios when the turbine spacing is small, for example, at 270°. Moreover, due to the limited number of turbines per row, the power ratios do not always reach an asymptotic behavior far downstream in the transect. Instead, they decrease monotonically. For a wind sector of ±5°, the highest error in power estimates occurs for the second turbine of the row. On the other hand, for wind sectors of ±10° and ±15°, the difference between second-row turbine power prediction and data reduces and the models well capture the power ratio trend along the transect. To better illustrate the models' performance, Figure 9 displays the distribution of the difference in power ratio between models' predictions and SCADA data shown in Figure 8, which is computed as

$$\Delta_{M-M} = \frac{P_{n,\text{Model}}}{P_{1,\text{Model}}} - \frac{P_{n,\text{Measured}}}{P_{1,\text{Measured}}} \tag{30}$$

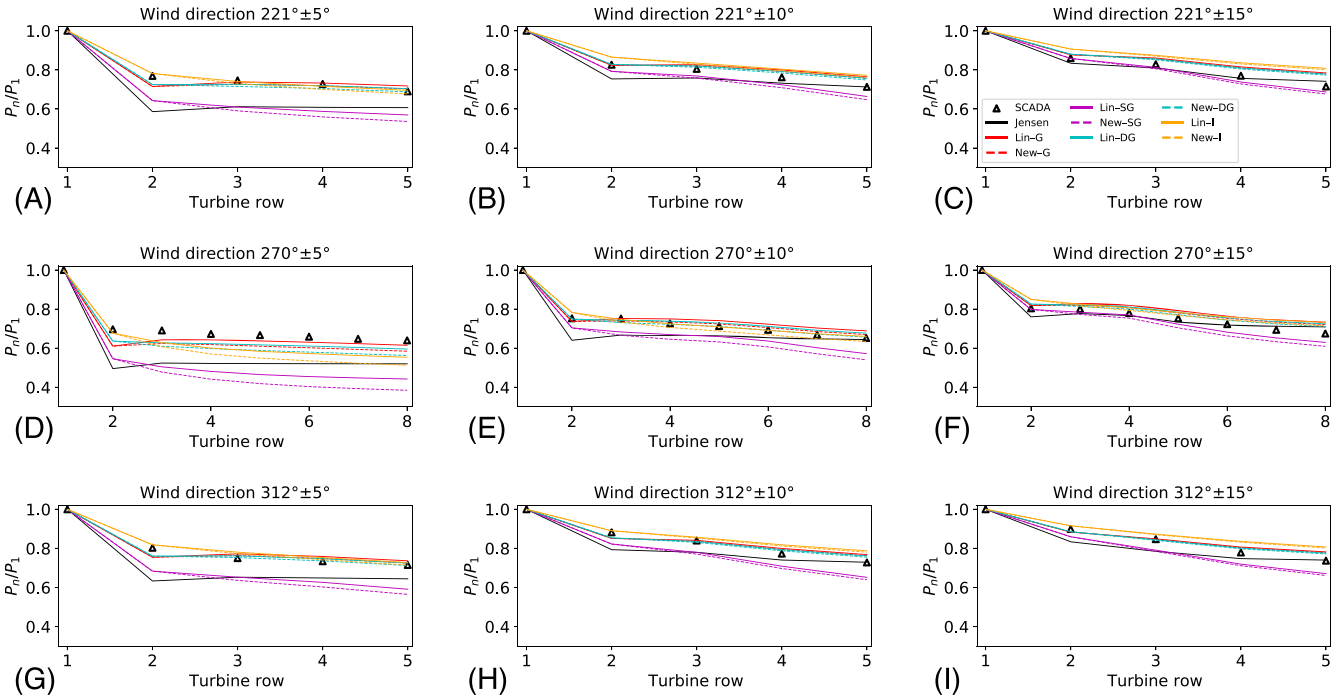

FIGURE 8 Power ratios for a wind sector of (left column) ±5°, (middle column) ±10° and (right column) ±15° centered on a mean wind direction of (top row) 221°, (middle row) 270° and (bottom row) 312° for the Horns Rev wind farm. The power ratios are averaged over the respective wind sector using a 1° increment and are further averaged over the wind speed range 8±0.5 m/s using increments of 0.5 m/s

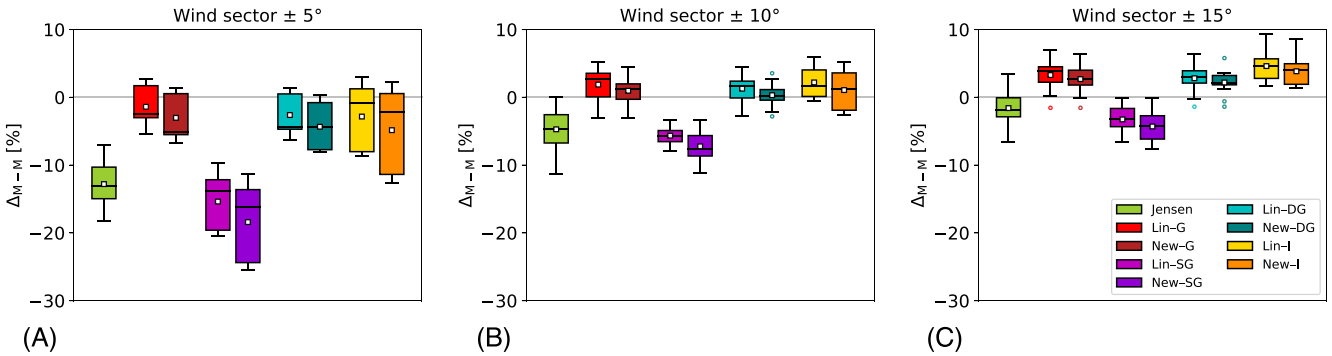

FIGURE 9 Distribution of the difference in power ratio between models' predictions and SCADA data for a wind sector of (A) ±5°, (B) ±10°, and (C) ± 15° centered on three mean wind directions (221°, 270° and 312°) for the Horns Rev wind farm. The power ratios are computed as in Figure 8. The box bounds the IQR. The horizontal black line and the white square denote the median and the mean, respectively. The whiskers extend to a maximum of 1.5×IQR beyond the box. The dots represent outliers

where $P_{n,\,Model}$ and $P_{n,\,Measured}$ represent the modeled and measured turbine power, respectively ($n = 1$ denotes a front-row turbine). For instance, Figure 9A displays the distribution of Δ_{M-M} encompassing the wind directions 221° ±5°, 270° ±5° and 312° ±5°. Note that Δ_{M-M} is always zero for a front-row turbine; hence, this value is not included in the statistics. All engineering wake models underestimate the power ratio if a narrow wind sector is considered, as shown in Figure 9A. A similar behavior was already observed in Figure 7A. However, if wider wind sectors are used, the models' predictions are more accurate, with biases closer to zero and narrower IQRs, as displayed in Figure 9B,C. These tendencies were also noticed by Barthelmie et al.[55] As shown in Appendix A1, the new wake-merging method predicts slightly higher velocity deficits than the linear superposition method. Moreover, the difference in velocity deficits between the two methods and the turbine spacing are inversely proportional. Since the linear superposition method already predicts lower turbine power outputs than SCADA data for a wind sector of ±5°, the new wake-merging method provides worse predictions. However, an opposite trend is seen in Figure 9B,C. Overall, we can conclude that the two methods have similar performance. The most accurate single-wake models are again the Gaussian and double-Gaussian ones, which show error distributions with close to zero biases and small IQRs for wind sectors of ±10° and ±15°. In fact, the very similar wake profile in the far-wake region obtained with these two models, as shown in Figures 4B and 4D, makes them almost undistinguishable in terms of power outputs when $S_x > 4D$. Finally, the Jensen and the super-Gaussian wake models show a strong negative bias for wind sectors of ±5° and ±10°, with Δ_{M-M} values down to −18% and −25%. However, their performance improves considerably when the averages are computed over wider wind sectors. More information on the MAE and IQR of the Δ_{M-L} and Δ_{M-M} distributions are reported in Table 3.

4.2 | London array

The London Array, with a capacity of 630 MW, is located 20 km off the Kent coast in the United Kingdom. The farm characteristics are listed in Table 2 while the farm layout, consisting of turbine spacings of 5.4*D* and 8.3*D* for the north- and south-western wind directions, is displayed in Figure 10. The farm has 175 SWT-120-3.6 turbines installed. The thrust curve of this turbine is, e.g., available at wind-turbine-models.com[51] while the power curve is, for example, accessible at The-Wind-Power.com[52] and are shown in Figure 5. The SCADA data are available in Nygaard[43] and consist in power ratios measured at two different wind speeds (6 ± 0.5 and 9 ± 0.5 m/s) for four different transects (the ones in black, orange, blue, and pink in Figure 10). The ambient turbulence intensity is measured by a met mast located upstream of the farm. The observed values are reported in Nygaard.[43] Note that the farm is located in proximity of a complex-shaped coastline. Therefore, the SCADA data could be affected by streamwise and/or spanwise velocity gradients induced by the different surface roughness between land and see surfaces. These coastal gradients could have some impacts on the power ratios comparison performed in this section, since the analytical flow models only use a homogeneous background velocity—no other data are available.

Figure 11A–D display the modeled and observed power ratios for the four transects at a wind speed of 6 ± 0.5 m/s. The power ratios are averaged over a wind sector of ±15° using a 1° increment and are further averaged over the wind speed range 6 ± 0.5 m/s using increments of 0.5 m/s. For all transects, the observations show a modest power drop between the first and the second turbine of the row. As usually happens in large farms, the power ratios stabilize after approximately the tenth turbine of the row. As expected, the new wake-merging method predicts a slightly lower power ratio than the linear superposition method. The Gaussian, double-Gaussian and Ishihara models perform similarly and show a very good agreement with observations. The Jensen model underestimates the power output of the firsts turbines in the row, but it captures the asymptotic behavior in all transects. A different tuning of this model could possibly improve its performance (e.g., see Peña et al[56]), but this is not in the scope of the current manuscript. As for the Horns Rev farm, the super-Gaussian wake model strongly underestimates the power output in all transects, being on average 30% off from observations for the last turbine of the row.

The results obtained for a wind speed of 9 ± 0.5 m/s are shown in Figure 11E–H. It is worth to notice that the models' performance differ from the ones observed at 6 ± 0.5 m/s, showing that it is bad practice to judge the quality of a model using data of a single row of turbines or using a unique wind speed value, as often done in literature. In fact, although some models show good agreement with observations for the firsts turbines in the row, they all fail in capturing the asymptotic behavior reached far downstream in the transects. Figure 11G shows that the observed power ratios continue to drop through the array, in contrast to the previous cases. Nygaard[43] did not find robust evidence that such a drop could have been caused by the deep array effect[42,57] and instead suggested that this behavior is due to the differences in ambient turbulence intensity between the north- and south-western transects. The super-Gaussian model fits extremely well the observations in such conditions, however it performs poorly in all other cases.

To better summarize the models' performance, Figure 12 displays the distribution of the difference in power ratio between models' predictions and SCADA data shown in Figure 11. The error in power ratio for a front-row turbine is always zero, therefore it is not included in the statistics. The box plots enlight the very similar performance between the two different wake-merging methods. In fact, when combining the predictions of all single-wake models, the MAE for the linear and new wake-merging methods are of 5.7% and 6.6% for 6 ± 0.5 m/s and of 8.7% and 7.5% for 9 ± 0.5 m/s. Moreover, Figure 12 also shows that the predictions of the Gaussian, double-Gaussian and Ishihara wake models are in good agreement with SCADA data, particularly for a wind speed of 6 ± 0.5 m/s. In Table 3, we provide more information on the MAE and IQR of the Δ_{M-M} distributions.

TABLE 3 Mean absolute error (MAE) and interquartile range (IQR) of the Δ_{M-L} and Δ_{M-M} distributions for the Horns Rev, London Array and Westermost Rough farms

Wind farm	Data	Jensen MAE (IQR)	Lin-G MAE (IQR)	New-G MAE (IQR)	Lin-SG MAE (IQR)	New-SG MAE (IQR)	Lin-DG MAE (IQR)	New-DG MAE (IQR)	Lin-I MAE (IQR)	New-I MAE (IQR)
Horns Rev	LES	4.6 (−5.8,2.5)	2.3 (0.7,2.9)	2.5 (−0.3,2.9)	5.2 (−8.0,−0.8)	5.9 (−8.9,−0.7)	2.3 (−0.1,2.8)	2.5 (0.1,3.5)	4.7 (1.2,5.8)	5.0 (0.4,5.8)
	SCADA ±5°	13.3 (−15.9,−10.8)	3.2 (−3.9,1.3)	4.0 (−5.6,0.1)	15.3 (−19.4,−12.2)	18.1 (−23.9,−14.1)	3.5 (2.2,4.5)	4.5 (−7.7,−1.3)	4.0 (−7.7,1.2)	5.43 (−11.0,0.3)
	SCADA ±10°	4.7 (−6.7,−2.5)	2.5 (0.1,3.5)	1.8 (-0.3,1.2)	5.7 (-6.5,-4.9)	7.2 (-8.6,-5.6)	1.9 (-0.1,2.4)	1.2 (-0.4,1.1)	2.4 (0.1,4.0)	2.7 (-1.9,3.6)
	SCADA ±15°	2.7 (−2.9,−0.1)	3.5 (2.2,4.5)	2.9 (1.8,4.0	3.2 (-4.3,-1.6)	4.3 (-6.1,-2.7)	3.0 (2.1,3.9)	2.4 (1.8,3.2)	4.6 (2.8,5.7)	3.8 (1.9,4.9)
London Array	SCADA 6±0.5 m/s	5.9 (−9.7,−0.7)	2.8 (-3.1,1.1)	3.3 (-5.4,-0.5)	13.4 (-17.0,-10.2)	15.4 (-19.2,-12.4)	2.9 (-4.0,0.1)	3.9 (-6.2,-1.5)	3.5 (-2.3,3.8)	3.8 (-5.3,2.5)
	SCADA 9±0.5 m/s	6.9 (2.6,7.9)	9.2 (6.1,10.7)	7.6 (5.1,8.8)	5.1 (-6.4,3.1)	6.1 (-9.6,1.0)	8.4 (6.2,9.6)	6.7 (4.0,8.1)	11.9 (8.8,11.1)	9.8 (6.2,10.0)
Westermost Rough	Dual-Doppler radar	11.2 (9.4,11.9)	9.3 (7.4,11.4)	3.3 (0.0,3.2)	9.3 (-11.8,-1.5)	14.6 (-19.5,-8.7)	10.6 (8.6,11.6)	4.9 (-0.3,4.8)	12.5 (9.9,13.2)	6.1 (1.4,7.8)

Note: The first and second value within the round brackets denote the first and third quartile, respectively. The results are expressed in percentage points.

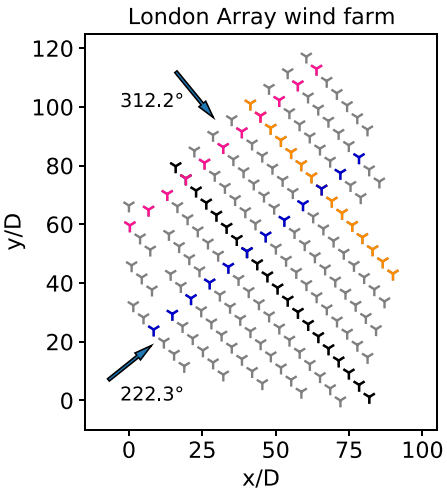

FIGURE 10 Layout of the London Array farm with distances normalized by the rotor diameter. The transects for which SCADA data are available are marked in black and orange for the north-western transects (312.2°) and in blue and pink for the south-western ones (222.3°)

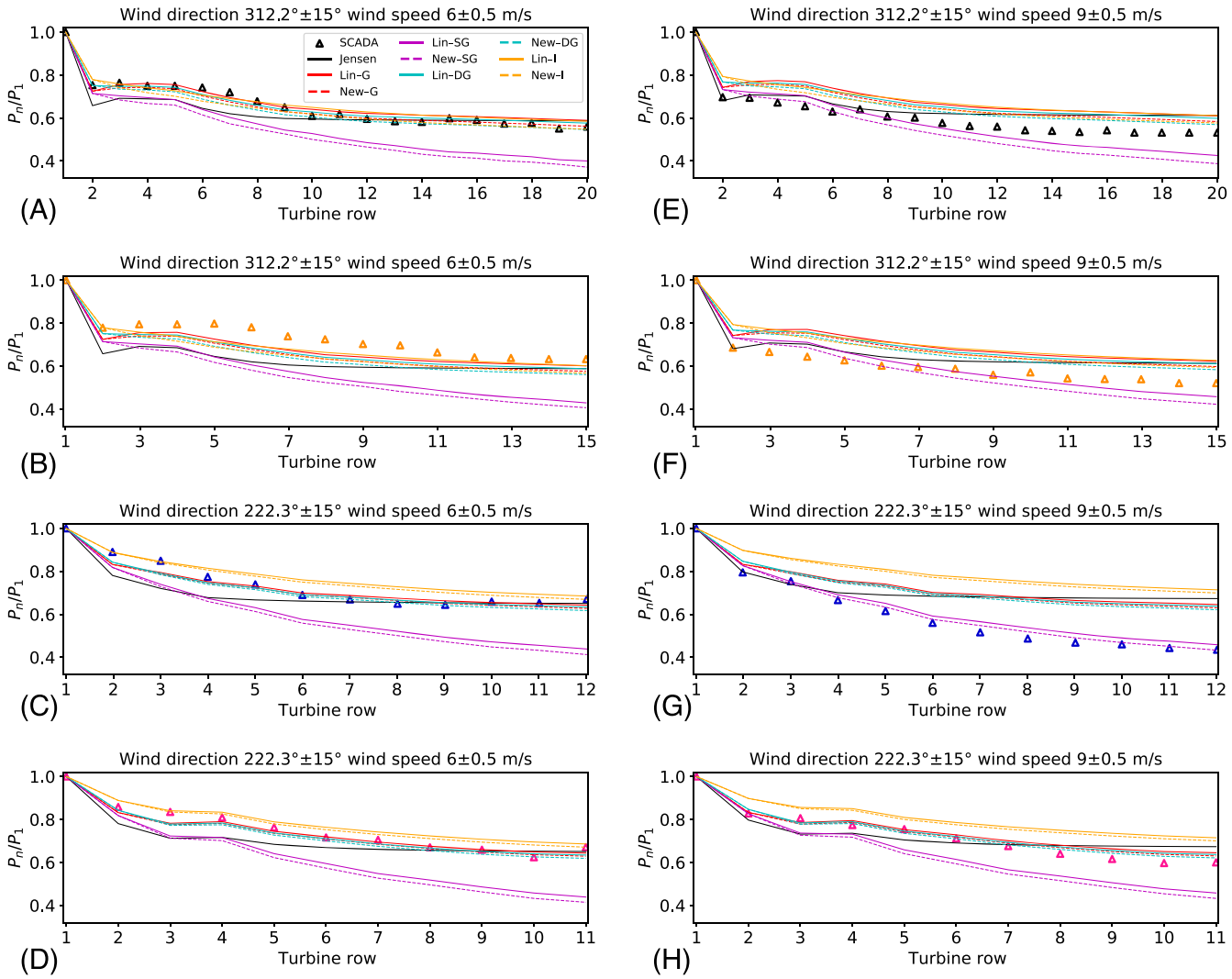

FIGURE 11 Power ratios along the north-western (312.2°) and south-western transects (222.3°). The power ratios are averaged over a wind sector of ± 15° using a 1° increment and are further averaged over the wind speed range (A–D) 6±0.5 m/s and (E–H) 9±0.5 m/s using increments of 0.5 m/s

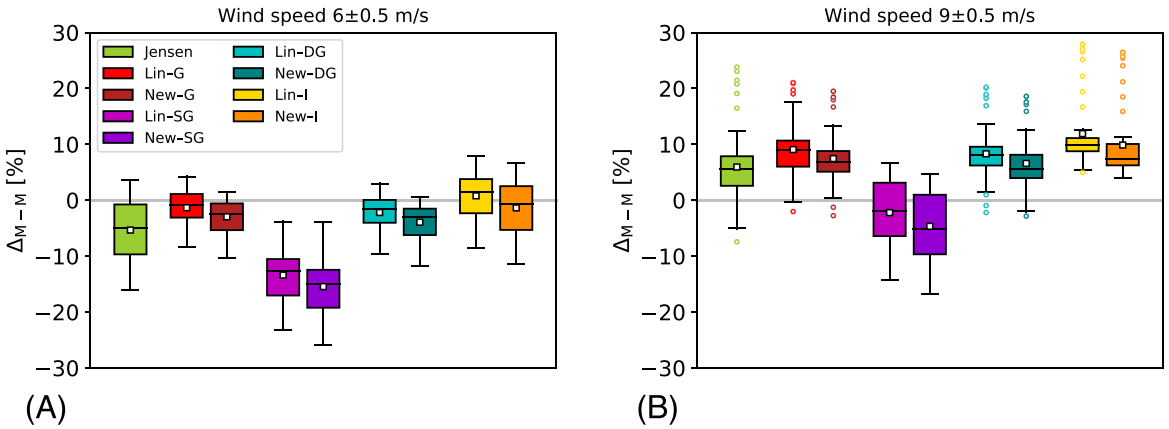

FIGURE 12 Distribution of the difference in power ratio between models' predictions and SCADA data for a wind speed of (A) 6 ± 0.5 and (B) 9 ± 0.5 m/s for the London Array wind farm. The power ratios are computed as in Figure 11. The box bounds the IQR. The horizontal black line and the white square denote the median and the mean, respectively. The whiskers extend to a maximum of 1.5×IQR beyond the box. The dots represent outliers

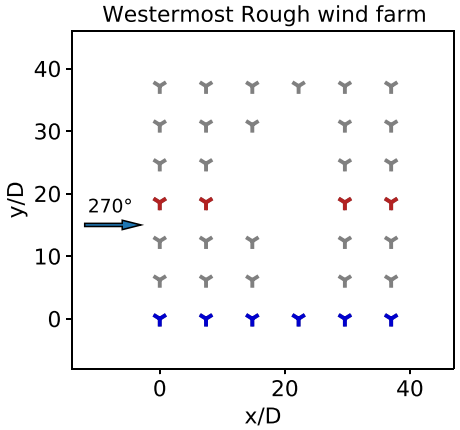

FIGURE 13 Layout of the Westermost Rough farm with distances normalized by the rotor diameter. The transects for which models' predictions are compared with dual-Doppler data are marked in blue (row 1) and red (row 4). Both transects are normal to the shore line

4.3 | Westermost rough

The Westermost Rough farm, located 8 km off the Holderness coast in the United Kingdom, became operational in May 2015. The farm employs 35 SWT-154-6.0 turbines, one of the largest offshore turbine to date with rotor diameter D= 154 m and hub height z_h= 106 m. The SWT-154-6.0 turbine thrust and power curves are shown in Figure 5 while the farm layout and characteristics are shown in Figure 13 and Table 2, respectively. In addition to the comparison between modeled and observed power ratios, we will asses the quality of the models also by analyzing the velocity fields through the farm and in its wake. The observation data are provided by Nygaard and Newcombe[36] and consist of dual-Doppler radar wind speed at a horizontal plane at hub height. The data are averaged over a time window of 1 hr. The velocity field is reconstructed from 3 to 32 km from the shore (streamwise direction) and for 20 km in a direction parallel to the shore (spanwise direction). Therefore, the entire flow field in and around the farm, which is approximately 7 × 7 km^2, is available. However, we will compare the models' predictions only with two transects of the dual-Doppler data which span from 2 km upstream to 16 km downstream of the farm, running across the first and fourth row of turbines. Two additional transects with a width of 250 m run parallel and on both sides of the farm at a distance of 10D from the first and last row of turbines. At each downstream distance, the velocity is averaged over these bands. Since these two transects do not cross the farm (and its wake), the resulting velocity is referred to as freestream or background velocity. Note that all transects are normal to the shore line. To obtain the freestream velocity across the first and fourth rows of turbines, Nygaard and Newcombe[36] used a linear interpolation between the two freestream transects. As a result, the background wind speed at row 1 and row 4 is slightly different. Moreover, the authors quantified

the uncertainty of the dual-Doppler measurements through a comparison with a co-located scanning lidar. They found out that the uncertainty is less than 0.2 m/s inside the wind farm and its wake, reaching a maximum of 0.8 m/s on the edges of the domain scanned by the lidar. Finally, the ambient turbulence intensity is fixed to 5.9% which corresponds to the value reported by Nygaard et al.[45] A plot of the dual-Doppler radar wind speed at hub height and more details about the measurement campaign are reported in Nygaard and Newcombe.[36]

Figure 14 shows the freestream velocity and the dual-Doppler wind speed measurements along transects which run through the first and fourth row of the farm together with the models' predictions. To not overcomplicate the plot, we show the streamwise velocity of only two wind-farm models, i.e. linear superposition and the new-wake merging method coupled with the Gaussian wake model (Lin-G and New-G). Note that the wind speed computed with the models is averaged over an imaginary rotor with the same diameter as the turbines disk at each point along the streamwise direction. The freestream velocity takes a quasi-constant value of 10.4 m/s in the farm induction region and it slightly decreases down to 10 m/s at the end of the farm. However, far downstream, the freestream velocity gradually increases up to 11.3 m/s. Since the farm is located only 8 km from the shore, the increase in freestream velocity is attributed to a coastal gradient. Note that the freestream velocity, which is interpreted as background velocity in our study, only varies by approximately 0.4 m/s within the farm. The dual-Doppler wind speed along the blue and red transects show the typical sawtooth behavior with maxima and minima located upstream and downstream of the turbines. The velocity reduction upstream of the third turbine of row 4 is attributed to axial induction. A similar behavior is also observed for the first turbine of row 1 and 4. The Lin-G model does not account for spatially varying background velocity. Instead, it relies on a global wind speed value measured several hundreds of meters upstream of the farm, which we fix to 10.4 m/s. On the other hand, the New-G model uses the spatially varying freestream velocity as input. The two predictions begin to diverge from the second turbine of the row. In fact, the Lin-G model overestimates the velocity at turbine locations in both row 1 and 4. Contrarily, the New-G model shows very good agreement with observations. Also, the wind speed far downstream the farm converges to the freestream velocity and not to the upstream wind speed value, which is more realistic. However, in this region, the Lin-G model's predictions are closer to the observations than the ones obtained with the New-G model. This could be due to a poor estimation of the freestream velocity in the far-wake region or to an underestimation of the velocity deficits computed with the Gaussian wake model. Finally, note that the Gaussian wake model does not conserve momentum in the near-wake region. For this reason, the model's predictions are plotted only in the far-wake regions, which corresponds to the region of interest of our study.

A two-dimensional plot displaying the freestream velocity at hub height is shown in Figure 15A, where the increase in wind speed along the streamwise direction is noticeable. Note that we plot the background velocity interpolated along the transect which crosses the fourth row of turbines and we assume it constant along the spanwise direction. Moreover, the velocity field is normalized by the wind speed measured 2*D* upstream of the farm. Next, Figure 15B,C illustrates the velocity at a horizontal plane at hub height obtained with the Lin-G and New-G models, respectively. Since both wake-merging methods are coupled with the same single-wake model, the observed differences only reside in how the methods overlap preceding wakes and deal with the freestream velocity.

Finally, we compute the differences in power ratio using Equation (30). Note that SCADA data are not available for this case study. Hence, $P_{n,\,\mathrm{Measured}}$ is computed using the turbine power curve where the velocity input refers to the turbine inflow velocity (i.e., the observed velocity in

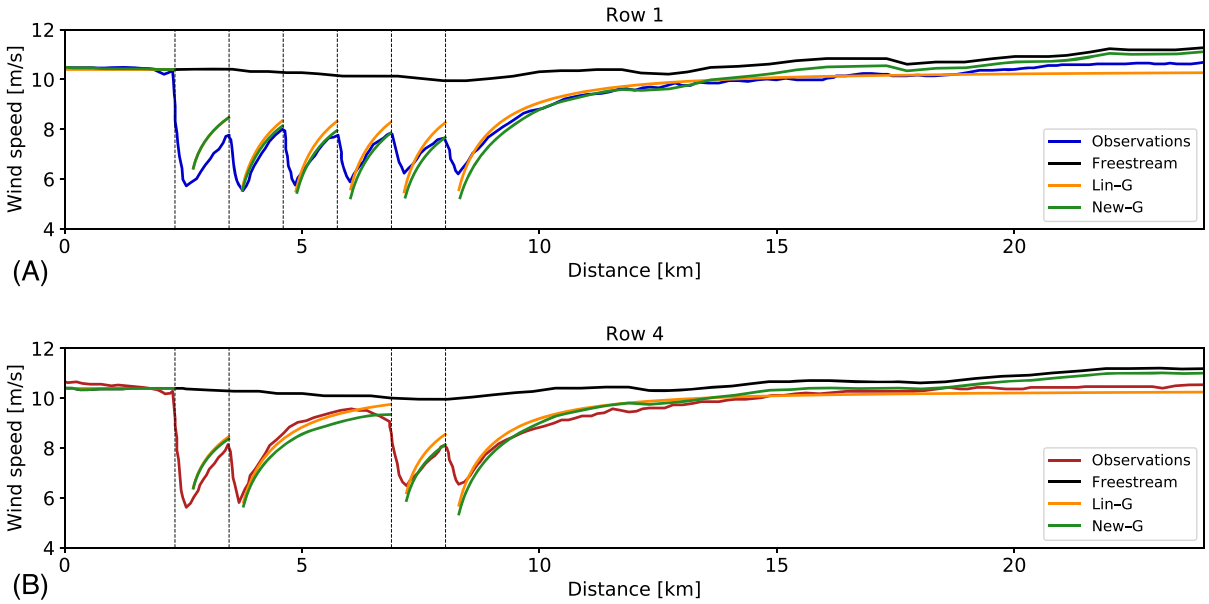

FIGURE 14 One-hour averaged dual-Doppler wind speed, freestream velocity and velocity predicted with the linear (Lin-G) and the new (New-G) wake-merging method coupled with the Gaussian wake model for the (A) blue and (B) red transects. All transects are normal to the shore line. The vertical dashed lines indicate the turbine positions

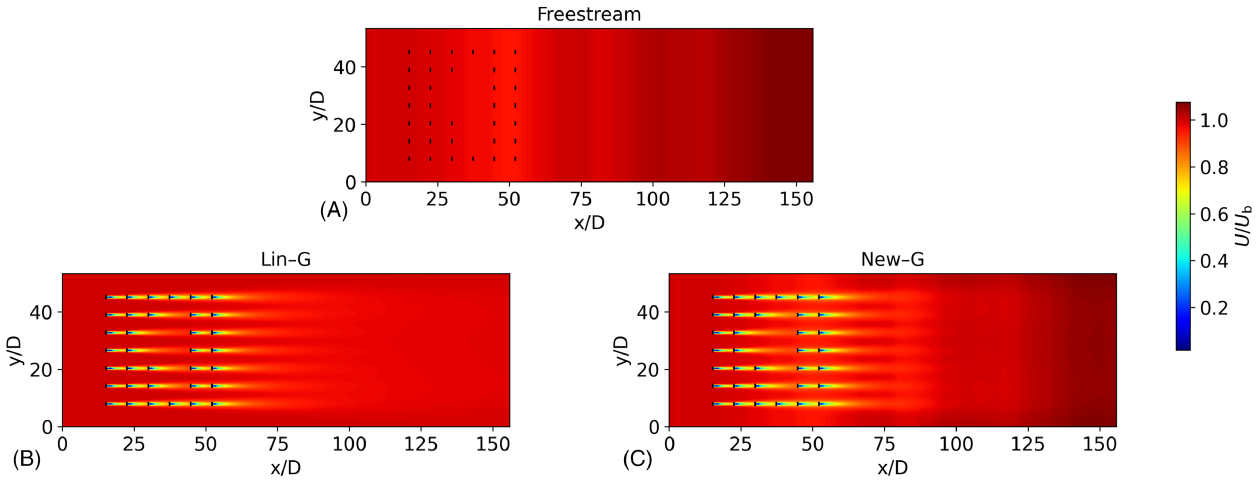

FIGURE 15 Top view of the (A) freestream wind speed and (B,C) velocity field computed with the linear and new wake-merging method coupled with the Gaussian wake model, respectively. The velocity is normalized by the wind speed measured 2*D* upstream of the Westermost Rough farm and is visualized at a horizontal plane at hub height. The *x* and *y* direction are normal and parallel to the shore line, respectively. The black lines denote the wind-turbine rotor locations

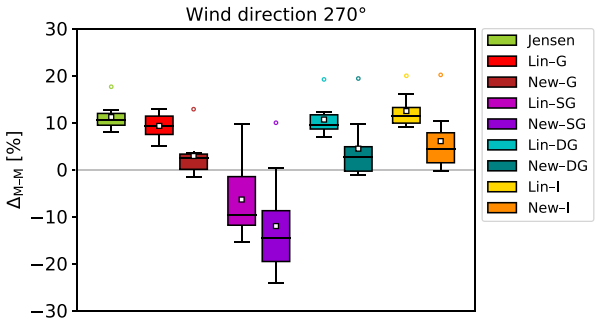

FIGURE 16 Distribution of the difference in power ratio between models' predictions and dual-Doppler data for the Westermost Rough wind farm. The box bounds the IQR. The horizontal black line and the white square denote the median and the mean, respectively. The whiskers extend to a maximum of 1.5×IQR beyond the box. The dots represent outliers

correspondence of the vertical dashed lines in Figure 14A,B). For completeness, we have included all wind-farm models in this analysis. The results are shown in Figure 16. Overall, the new wake-merging method outperforms the linear superposition one. In fact, since the freestream velocity decreases over the wind-farm area, the new model predicts lower turbine power outputs, showing biases closer to zero than the ones obtained with the linear method, which are on average 10% off from observations. As in the previous analysis, the Lin-SG model strongly underestimates the turbine power outputs. Consequently, in light of the above reasoning, the New-SG model shows an even higher bias. However, we believe that a different tuning of the super-Gaussian wake model would reduce the bias, but this is out of the scope of the current manuscript. When clustering the predictions of all single-wake models, the linear and new wake-merging methods show a MAE of 10.5% and 7.2%, respectively. More information on the MAE and IQR of the Δ_{M-M} distributions are reported in Table 3. The better agreement with observations achieved with the new wake-merging method (except when coupled with the super-Gaussian wake model) once again points out the importance of accounting for a spatially varying background velocity when doing energy yield assessments.

5 | CONCLUSIONS

In the current study, we proposed a new wake-merging method for predicting wake losses and farm power output. The waked flow through the farm is expressed in conjunction with a spatially varying background velocity. Hence, the new superposition method does not rely on a global wind-speed value, which is usually taken upstream of the farm. Instead, it superimposes the wake velocity deficits generated by turbines on a heterogeneous velocity field. This is of fundamental importance for achieving better farm power predictions and consequently more accurate annual energy yield assessments. In fact, the mesoscale horizontal velocity gradients that develop in coastal regions or in proximity of orographic features

make wind farms operating in velocity fields which are rarely uniform. The proposed superposition method is consistent with self-similarity in the wake of every turbine in the farm. Moreover, the new wake-merging method is momentum-conserving if the flow induced by preceding turbines at the location of a downwind turbine is quasi-homogeneous in the horizontal directions and if a slow varying background velocity is used.

LES results, Dual-Doppler radar measurements and SCADA data from the Horns Rev, London Array and Westermost Rough farm were used for validating the new wake-merging method. To this end, the new and the linear superposition methods were coupled with the Gaussian, super-Gaussian, double-Gaussian and Ishihara single-wake models. The Jensen model coupled with quadratic superposition was also included in the analysis, as an additional reference. A homogeneous background velocity field was used in the Horns Rev and London Array case studies. In such conditions, the distributions of the difference in power ratio between the new and linear superposition methods predictions and observations show a similar MAE and IQR, with the new wake-merging method predicting slightly higher velocity deficits. Next, a heterogeneous background velocity field was used in the Westermost Rough case study. The new wake-merging method predictions display a lower MAE with a similar IQR in such conditions, being overall more accurate than the ones obtained with linear superposition. The most accurate power predictions were provided by the Gaussian and double-Gaussian wake models, independently from the flow conditions. Despite being a data-driven model, the Ishihara model shows decent agreements with observation, partially underestimating the velocity deficits in most of the cases. The Jensen model showed a negative bias in power estimates for the majority of wind speeds and wind directions. The super-Gaussian wake model was the one that diverged the most from observations, underestimating the power output in most of the circumstances. We believe that a different tuning of the model coefficients, for example by minimizing the difference between predictions and LES results using a larger weight on the error in the far-wake than in the near-wake region, could improve its performance.

Future research will focus on a more extensive validation of the proposed wake-merging method in presence of heterogeneous background velocity fields. To do so, a combination of ERA5 data, met mast and lidar measurements and mesoscale simulations in the region around a farm of interest (prior to its construction) could be used, to estimate the yearly variation of wind conditions and turbulence intensity. This procedure would allow to compute the background velocity fields over a certain time span. Next, these fields can be used as inputs by the new wake merging-method, which will provide an energy yield estimate. After the construction of the farm, it will be more challenging to define a background velocity field and interpolation techniques similar to the ones used in Djath et al[5] and Nygaard and Newcombe[36] could be adopted. For instance, the Anholt wind farm is a suitable candidate for this type of study due to the strong coastal gradients present in its location.[4,58] Also, the new wake-merging method can account for velocity gradients generated by self-induced gravity waves. Hence, we plan to couple the new wind-farm model with the recently developed mid-fidelity three-layer model[34] in the future. Finally, yaw effects will be included in the model formulation. To further improve the performance of wake engineering models, a more general parametrization of the wake growth rate is necessary. Moreover, the inclusion of axial induction effects would improve the models reliability and representation of reality in the vicinity of turbines.

ACKNOWLEDGEMENTS

The authors acknowledge support from the Research Foundation Flanders (FWO, grant no. G0B1518N), and from the project FREEWIND, funded by the Energy Transition Fund of the Belgian Federal Public Service for Economy, SMEs, and Energy (FOD Economie, K.M.O., Middenstand en Energie).

CONFLICT OF INTEREST

The authors declare that they have no conflict of interest.

AUTHOR CONTRIBUTIONS

L.L. and J.M. jointly developed the new wake-merging method and set up the simulation studies. L.L. performed code implementations and carried out the simulations. L.L. and J.M. jointly wrote the manuscript.

PEER REVIEW

The peer review history for this article is available at https://publons.com/publon/10.1002/we.2669.

ORCID

Luca Lanzilao https://orcid.org/0000-0003-1976-3449
Johan Meyers https://orcid.org/0000-0002-2828-4397

REFERENCES

1. Barthelmie RJ, Badger J, Pryor SC, Hasager CB, Christiansen MB, Jrgensen BH. Offshore coastal wind speed gradients: issues for the design and development of large offshore windfarms. *Wind Engng*. 2007;31 (6):369-382.
2. Van der Laan MP, Pea A, Volker P, Hansen KS, Srensen MN, Hasager CB. Challenges in simulating coastal effects on an offshore wind farm. *J Phys Conf Ser*. 2017;854:12046. https://doi.org/10.1088/1742-6596/854/1/012046

3. Durran DR. Mountain waves and downslope winds. *In Atmospheric Processes Over Complex Terrain*. Boston, MA: American Meteorological Society; 1990:59-81.
4. Ahsbahs T, Badger M, Volker P, Hansen KS, Hasager CB. Applications of satellite winds for the offshore wind farm site anholt. *Wind Energ Sci*. 2018;3:573-588. https://doi.org/10.5194/wes-3-573-2018
5. Djath B, Schulz-Stellenfleth J, Caadillas B. Impact of atmospheric stability on x-band and c-band synthetic aperture radar imagery of offshore windpark wakes. *J Renew Sustain Energy*. 2018;10:43301. https://doi.org/10.1063/1.5020437
6. Ahsbash T, Nygaard NG, Newcombe A, Badger M. Wind farm wakes from sar and doppler radar. *Remote Sensing*. 2020;12:462. https://doi.org/10.3390/rs12030462
7. Lissaman PBS. Energy effectiveness of arbitrary arrays of wind turbines. *J Energy*. 1979;3(6):323-328.
8. Katic I, Hjstrup J, Jensen N. A simple model for cluster efficiency, In: Proceedings of the European Wind Energy Association Conference and Exhibition; 1986:407-410. Rome, Italy.
9. Voutsinas S, Rados K, Zervos A. On the analysis of wake effects in wind parks. *Wind Engng*. 1990;14(4):204-219.
10. Niayifar A, Porté-Agel F. Analytical modeling of wind farms: a new approach for power prediction. *Energies*. 2016;9:741. https://doi.org/10.3390/en9090741
11. Jensen NO. A note on wind generator interaction. Technical report Ris-M-2411, Roskilde, Denmark, Risø National Laboratory; 1983.
12. Bastankhah M, Porté-Agel F. A new analytical model for wind-turbine wakes. *Renew Energy*. 2014;70:116-123.
13. Gonzlez JS, Rodriguez AGG, Mora JC, Santos JR, Payan MB, Hjstrup J, Thgersen M. Optimization of wind farm turbines layout using an evolutive algorithm. *J Renew Energy*. 2010;35(8):1671-1681. https://doi.org/10.1016/j.renene.2010.01.010
14. Pea A, Rthor PE, Van der Laan MP. On the application of the Jensen wake model using a turbulence-dependent wake decay coefficient: the sexbierum case. *Wind Energy*. 2016;19:763-776. https://doi.org/10.1002/we.1863
15. Hassan G, Ltd P. Gh windfarmer theory manual; 2009.
16. Truepower AWS. Openwind theoretical basis and validation; 2010.
17. Frandsen S, Barthelmie RJ, Pryor S, Rathmann O, Larsen S, Hjstrup J, Thgersen M. Analytical modelling of wind speed deficit in large offshore wind farms. *Wind Energy*. 2006;9:39-53. https://doi.org/10.1002/we.189
18. Tennekes H, Lumley JL. *A first course in turbulence*. Cambridge, UK: The MIT Press; 1972.
19. Anderson JD. *Fundamentals of aerodynamics*. McGraw-Hill; 2011.
20. Xiaoxia G, Hongxing Y, Lin L. Optimization of wind turbine layout position in a wind farm using a newly-developed two-dimensional wake model. *Appl Energy*. 2016;174:192-200. https://doi.org/10.1016/j.apenergy.2016.04.098
21. Parada L, Herrera C, Flores P, Parada V. Wind farm layout optimization using a gaussian-based wake model. *Renew Energy*. 2017;107:531-541. https://doi.org/10.1016/j.renene.2017.02.017
22. Shapiro CR, Starke GM, Meneveau C, Gayme DF. Wake modeling paradigm for wind farm design and control. *Energies*. 2019;12:15. https://doi.org/10.3390/en12152956
23. Blondel F, Cathelain M. An alternative form of the super-gaussian wind turbine wake model. *Wind Energy Sci*. 2020;5:1225-1236. https://doi.org/10.5194/wes-2019-99
24. Schreiber J, Balbaa A, Bottasso CL. Brief communication: a double-Gaussian wake model. *Wind Energy Sci*. 2020;5:237-244. https://doi.org/10.5194/wes-5-237-2020
25. Keane A, Aguirre PEO, Ferchland H, Clive P, Gallacher D. An analytical model for a full wind turbine wake. *J Phys: Conf Ser*. 2016;753:32039. https://doi.org/10.1088/1742-6596/753/3/032039
26. Ishihara T, Qian GW. A new gaussian-based analytical wake model for wind turbines considering ambient turbulence intensities and thrust coefficient effects. *J Wind Eng Ind Aerod*. 2018;177:275-292. https://doi.org/10.1016/j.jweia.2018.04.010
27. Schreiber J, Bottasso CL, Salbert B, Campagnolo F. Improving wind farm flow models by learning from operational data. *Wind Energ Sci*. 2020;5:647-673. https://doi.org/10.5194/wes-5-647-2020
28. Brogna R, Feng J, Srensen JN, Shen WZ, Porté-Agel F. A new wake model and comparison of eight algorithms for layout optimization of wind farms in complex terrain. *Appl Energy*. 2020;259:114189. https://doi.org/10.1016/j.apenergy.2019.114189
29. Farrell A, King J, Draxl C, Mudafort R, Hamilton N, Bay CJ, Fleming P, Simley E. Design and analysis of a spatially heterogeneous wake. *Wind Energy Sci*. 2021;6:737-758. https://doi.org/10.5194/wes-6-737-2021
30. Shamsoddin S, Porté-Agel F. A model for the effect of pressure gradient on turbulent axisymmetric wakes. *J Fluid Mech*. 2018;837:R3. https://doi.org/10.1017/jfm.2017.864
31. Bastankhah M, Porté-Agel F. Experimental and theoretical study of wind turbine wakes in yawed conditions. *J Fluid Mech*. 2016;806:506-541. https://doi.org/10.1017/jfm.2016.595
32. Qian GW, Ishihara T. A new analytical wake model for yawed wind turbines. *Energies*. 2018;11:665. https://doi.org/10.3390/en11030665
33. Holoborodko P. Cubature formulas for the unit disk. 2011. http://www.holoborodko.com/pavel/numerical-methods/numericalintegration/cubature-formulas-for-the-unit-disk/
34. Allaerts D, Meyers J. Sensitivity and feedback of wind-farm induced gravity waves. *J Fluid Mech*. 2019;862:990-1028.
35. Crespo A, Hernandez J. Turbulence characteristics in wind-turbine wakes. *J Wind Eng Ind Aerodyn*. 1996;61:71-85. https://doi.org/10.1016/0167-6105(95)00033-X
36. Nygaard NG, Newcombe AC. Wake behind an offshore wind farm observed with dual-doppler radars. *J Phys: Conf Ser*. 2018;1037:72008. https://doi.org/10.1088/1742-6596/1037/7/072008
37. Tennekes H. The logarithmic wind profile. *Int J Atmos Sci*. 1973;30:234-238.
38. Wu KL, Porté-Agel F. Flow adjustment inside and around large finite-size wind farms. *Energies*. 2017;10:2164. https://doi.org/10.3390/en10122164
39. Allaerts D, Meyers J. Boundary-layer development and gravity waves in conventionally neutral wind farms. *J Fluid Mech*. 2017;814:95-130.
40. Zong H, Porté-Agel F. A momentum-conserving wake superposition method for wind farm power prediction. *J Fluid Mech*. 2020;889:A8. https://doi.org/10.1017/jfm.2020.77
41. Cleve J, Greiner M, Enevoldsen P, Birkemose B, Jensen L. Model-based analysis of wake-flow data in the nysted offshore wind farm. *Wind Energy*. 2009;12(2):125-135. https://doi.org/10.1002/we.314

42. Barthelmie RJ, Jensen LE. Evaluation of wind farm efficiency and wind turbine wakes at the nysted offshore wind farm. *Wind Energy*. 2010;13(6):573-586. https://doi.org/10.1002/we.408
43. Nygaard NG. Wakes in very large wind farms and the effect of neighbouring wind farms. *J Phys: Conf Ser*. 2014;524:12162. https://doi.org/10.1088/1742-6596/524/1/012162
44. Duc T, Coupiac O, Girard N, Giebel G, Gmen T. Local turbulence parameterization improves the Jensen wake model and its implementation for power optimization of an operating wind farm. *Wind Energ Sci*. 2019;4:287-302. https://doi.org/10.5194/wes-4-287-2019
45. Nygaard NG, Steen ST, Poulsen L, Pedersen JG. Modelling cluster wakes and wind farm blockage. *J Phys: Conf Ser*. 2020;1618:62072. https://doi.org/10.1088/1742-6596/1618/6/062072
46. Cathelain M, Blondel F, Joulin PA, Bozonnet P. Calibration of a super-gaussian wake model with a focus on near-wake characteristics. *J Phys: Conf Ser*. 2020;1618:62008. https://doi.org/10.1088/1742-6596/1618/6/062008
47. Virtanen P, Gommers R, Oliphant TE, Haberland M, Reddy T, Cournapeau D, Burovski E, Peterson P, Weckesser W, Bright. Scipy 1.0: fundamental algorithms for scientific computing in python. *Nature Methods*. 2020;17:261-272. https://doi.org/10.1038/s41592-019-0686-2
48. Frandsen S, Thøgersen ML. Integrated fatigue loading for wind turbines in wind farms by combining ambient turbulence and wakes. *J Wind Eng*. 1999;23:327-339. http://www.jstor.com/stable/43749903
49. Wu YT, Porté-Agel F. Atmospheric turbulence effects on wind-turbine wakes: an les study. *Energies*. 2012;5:5340-5362. https://doi.org/10.3390/en5125340
50. The-wind-power.com. Accessed March 14, 2021.
51. Wind-turbine-models.com. Accessed March 14, 2021.
52. The-wind-power.com. Accessed March 14, 2021.
53. Commissiemer.nl. Accessed March 14, 2021.
54. Porté-Agel F, Wu YT, Chen CH. A numerical study of the effects of wind direction on turbine wakes and power losses in a large wind farm. *J Energies*. 2013;6(10):5297-5313. https://doi.org/10.3390/en6105297
55. Barthelmie RJ, Hansen K, Frandsen ST, Rathmann O, Schepers JG, Schlez W, Phillips J, Rados K, Zervos A, Politis ES, Chaviaropoulus PK. Modelling and measuring flow and wind turbine wakes in large wind farms offshore. *Wind Energ*. 2009;12:431-444. https://doi.org/10.1002/we.348
56. Pea A, Rthor PE, Hasager CB, Hansen KS. Results of wake simulations at the horns rev i and lillgrund wind farms using the modified park model. DTU Wind Energy-E-Report-0026(EN); 2013.
57. Schlez W, Neubert A. A new developments in large wind farm modelling. EWEC 2009; 2009.
58. Pea A, Schaldemose K, Ott S, van der Laan MP. On wake modeling, wind-farm gradients, and aep predictions at the anholt wind farm. *Wind Energy Sci*. 2018;3:191-202. https://doi.org/10.5194/wes-3-191-2018

SUPPORTING INFORMATION

Additional supporting information may be found online in the Supporting Information section at the end of this article.

How to cite this article: Lanzilao L, Meyers J. A new wake-merging method for wind-farm power prediction in the presence of heterogeneous background velocity fields. *Wind Energy*. 2022;25(2):237-259. https://doi.org/10.1002/we.2669

APPENDIX A

COMPARISON BETWEEN LINEAR SUPERPOSITION OF VELOCITY DEFICITS AND NEW WAKE-MERGING METHOD

The aim of this section is to compare two different wake-merging methods, namely the one proposed by Niayifar and Porté-Agel[10] and the one derived in this manuscript. The linear superposition method does not support a varying background velocity field. Therefore, to conduct a fair comparison, we use a uni-directional homogeneous background flow.

First, let's consider a row of N_t turbines aligned with the flow direction. Following the derivation of Niayifar and Porté-Agel[10] and Allaerts and Meyers,[34] we can write the turbine inflow velocity of a generic turbine k as

$$u_k^{\mathrm{Lin}} = U_{\mathrm{b}} - \sum_{l=1}^{N_t} u_l^{\mathrm{Lin}} \overline{W}_{l\to k} \quad \text{with} \quad \overline{W}_{l\to k} = \sum_{q=1}^{N_q} \omega_q W_l(\boldsymbol{x}_{k,q}) \tag{A1}$$

where $W(\boldsymbol{x})$ is a generic wake deficit function, $\omega_q = 1/N_q$ is a weighting factor and $\boldsymbol{x}_{k,q}$ are the quadrature-point coordinates on the rotor disk of the turbine k chosen following the quadrature rule proposed by Holoborodko.[33] Moreover, $\bar{W}_{l\to k}$ denotes the wake deficit function of turbine l averaged over the rotor disk of turbine k. On the other hand, if we use Equation (11) together with Equation (17), the turbine inflow velocity of a generic turbine k computed with the new wake-merging method is expressed as

$$u_k^{\text{New}} = U_b \prod_{l=1}^{N_t} \left[1 - \bar{W}_{l\to k}\right]. \tag{A2}$$

If we set N_t=2, it is easy to show that $u_2^{\text{Lin}} = u_2^{\text{New}}$. However, for N_t=3, we have

$$u_3^{\text{Lin}} = U_b\left[1 - \bar{W}_{1\to 3} - \bar{W}_{2\to 3} + \bar{W}_{1\to 2}\bar{W}_{2\to 3}\right], \tag{A3}$$

$$u_3^{\text{New}} = U_b\left[1 - \bar{W}_{1\to 3} - \bar{W}_{2\to 3} + \bar{W}_{1\to 3}\bar{W}_{2\to 3}\right]. \tag{A4}$$

The only difference between Equations (A3) and (A4) is in the last term on the right hand side. Since $W(\boldsymbol{x})$ decreases monotonically with distance, $\bar{W}_{1\to 2} > \bar{W}_{1\to 3}$ which implies $u_3^{\text{Lin}} > u_3^{\text{New}}$. This simple example shows that the two wake-merging methods differ even when U_b is homogeneous. Moreover, it also illustrates that the new wake-merging method predicts higher velocity deficits than the linear superposition method in homogeneous conditions.

Next, we look at the difference in velocity fields predicted by the two methods. To this end, we fix U_b to 10 m/s with ambient turbulence intensity of 12%. Moreover, the turbine rotor diameter is D= 154 m and the turbine thrust set-point is C_T=0.85. Both methods are coupled with the Gaussian wake model. The difference between velocity fields is computed as

$$\mathcal{E}_U(\boldsymbol{x}) = \frac{U^{\text{New}}(\boldsymbol{x}) - U^{\text{Lin}}(\boldsymbol{x})}{U_b} \tag{A5}$$

where $U^{\text{New}}(\boldsymbol{x})$ and $U^{\text{Lin}}(\boldsymbol{x})$ denote the velocity through the farm predicted by the new and the linear superposition method, respectively. Figure A1 displays a side view of $\mathcal{E}_U(\boldsymbol{x})$ at the turbine centerline plane for a row of five turbines. Since the two wake-merging methods are analytically equal for a single turbine, the velocity fields are identical up to the second turbine of the row. However, the models clearly differ far downstream in the row. As expected, the new superposition method predicts a lower velocity through the farm specially for a small streamwise turbine spacing, as displayed in Figure A1A. In such case, $\mathcal{E}_U(\boldsymbol{x})$ reaches values down to -2.3%. Note that $\mathcal{E}_U(\boldsymbol{x})$ assumes positive values only in the near-wake region of the second turbine of the row. However, the thrust coefficients are written as an error function of the streamwise coordinate in this region,[40] since the Gaussian wake model is not momentum-conservative for $C_T > 8\sigma^2/D^2$ (which happens here when $0 < (x - x_k)/D < 1.5$). Therefore, the models' predictions are not relevant in this region. On the other hand, Figure A1C shows that the models' predictions become comparable when turbines are widely spaced (e.g., $\mathcal{E}_U \approx -0.2\%$ when $S_x = 10D$). In fact, the wake deficit function $W(\boldsymbol{x})$ converges to zero for large streamwise distances, reducing the differences between wake-merging methods predictions. Note that $\mathcal{E}_U(\boldsymbol{x})$ shows an axisymmetric distribution for all turbine spacings since we have not considered vertical shear and we have neglected ground-wake interactions.

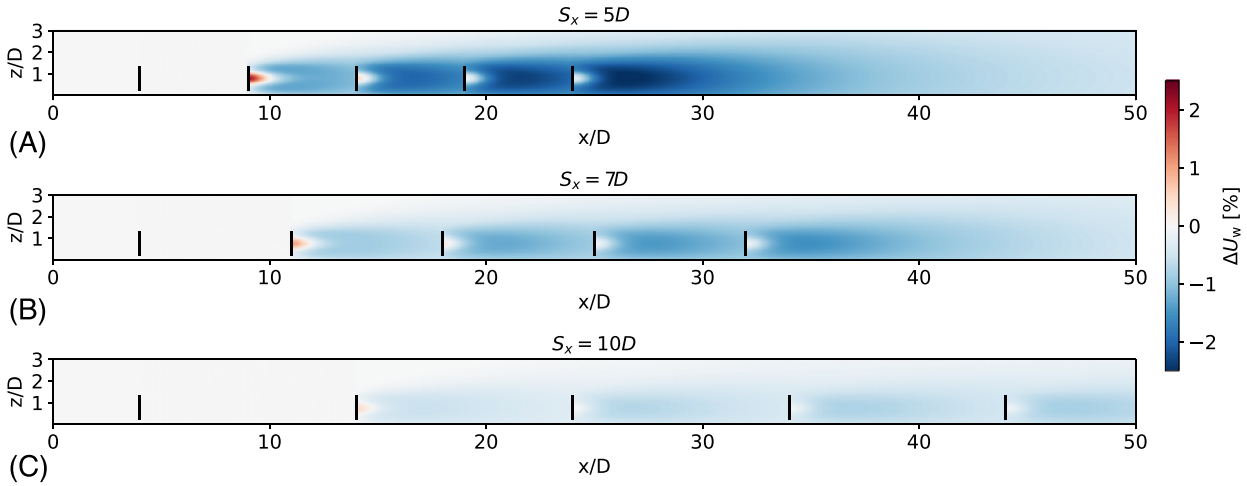

FIGURE A1 Difference between velocity fields computed with the new and the linear superposition method coupled with the Gaussian wake model. The difference is visualized at the turbine centerline plane for a turbine spacing of (A) 5*D*, (B) 7*D*, and (C) 10*D*. The black lines denote the wind-turbine rotor locations

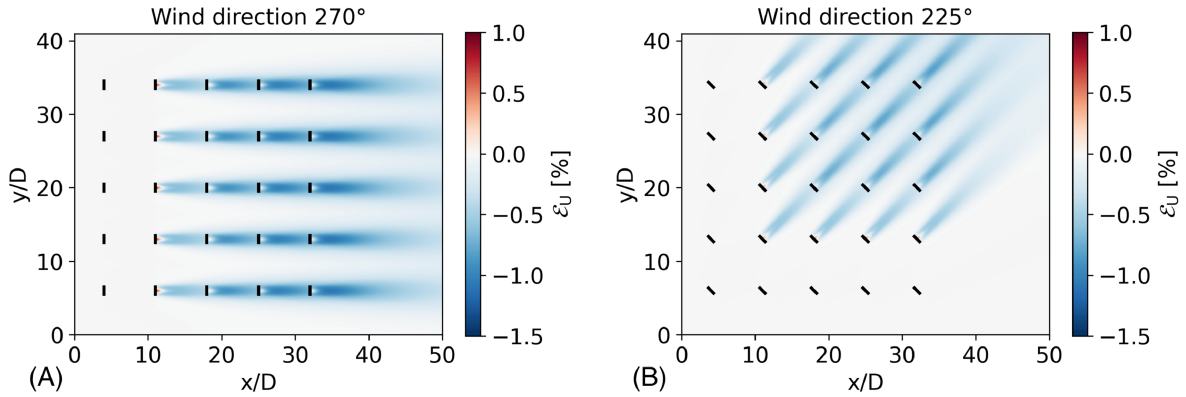

FIGURE A2 Difference between velocity fields computed with the new and the linear superposition method coupled with the Gaussian wake model. The difference is visualized at a horizontal plane at hub height for a wind direction of (A) 270° and (B) 225°. The black lines denote the wind-turbine rotor locations

Figure A2 illustrates the distribution of $\mathcal{E}_U(\boldsymbol{x})$ at a horizontal plane at hub height for a farm of 25 turbines with streamwise and spanwise spacings of $S_x = S_y = 7D$. The models setup and atmospheric conditions correspond to the ones detailed above. The new superposition method predicts a lower velocity than the linear one far downstream in the farm, specially through the centerline of the wakes where $\mathcal{E}_U \approx -1.5\%$. As mentioned above, there is no difference between the two models up to the second turbine of the rows. Moreover, $\mathcal{E}_U(\boldsymbol{x})$ assumes lower values for a wind direction of 225° since the turbine spacing is larger than the one at 270°.